iScience

CellPress
OPEN ACCESS

Article

DDI2 protease controls embryonic development and inflammation via TCF11/NRF1

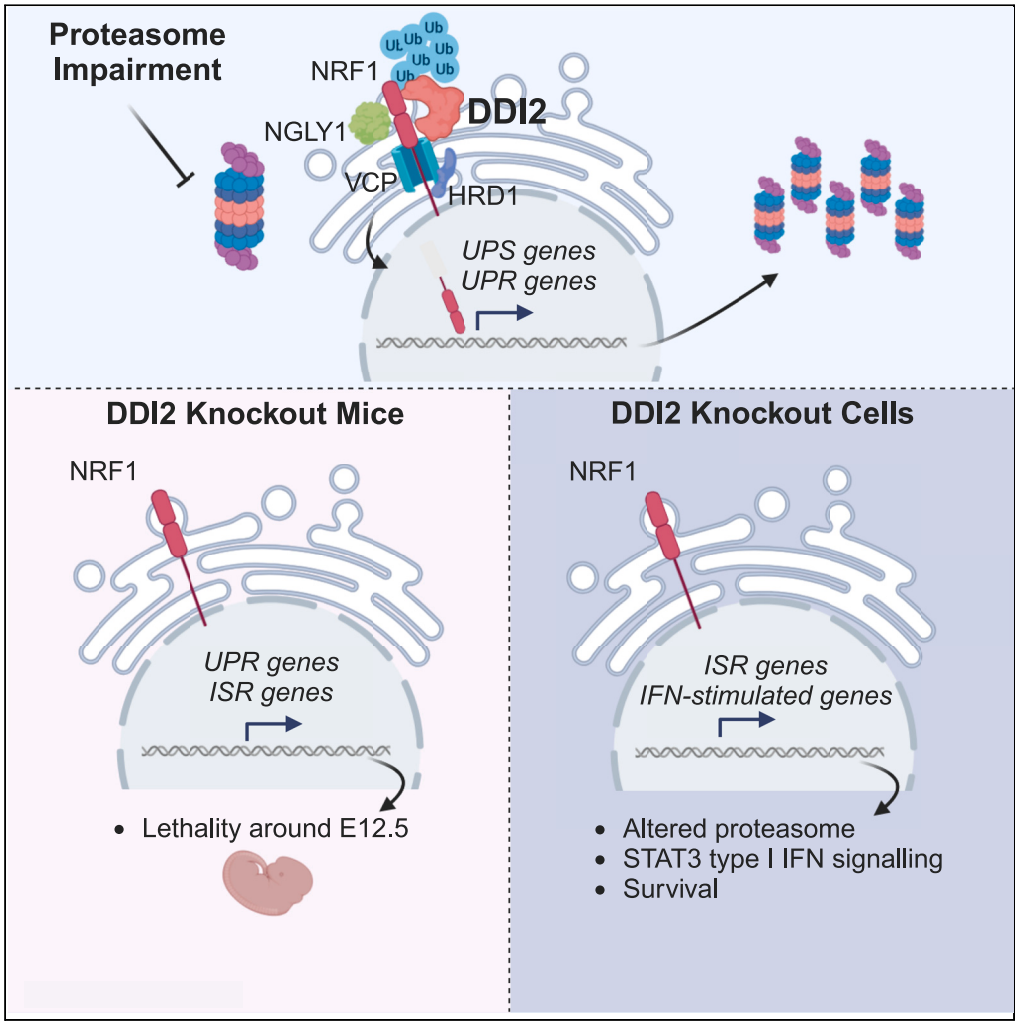

Monika Nedomova, Stefanie Haberecht-Müller, Sophie Möller, ..., Jan Konvalinka, Elke Krüger, Klara Grantz Saskova

elke.krueger@uni-greifswald.de (E.K.)
saskova2@natur.cuni.cz (K.G.S.)

Highlights

DDI2 failure in mice causes severe developmental defects and embryonic lethality

DDI2 dysfunction causes proteotoxic stress and proteasome impairment

DDI2 dysfunction induces the UPR and ISR signaling pathways

DDI2-deficient cells survive via activation of interferon and MAPK signaling

Nedomova et al., iScience 27, 110893
October 18, 2024
https://doi.org/10.1016/j.isci.2024.110893

iScience

CellPress
OPEN ACCESS

Article

DDI2 protease controls embryonic development and inflammation via TCF11/NRF1

Monika Nedomova,[1,2,3,7] Stefanie Haberecht-Müller,[4,7] Sophie Möller,[4] Simone Venz,[4] Michaela Prochazkova,[5] Jan Prochazka,[5] Frantisek Sedlak,[1,2,3] Kallayanee Chawengsaksophak,[6] Elke Hammer,[5] Petr Kasparek,[6] Michael Adamek,[1,3] Radislav Sedlacek,[6] Jan Konvalinka,[1] Elke Krüger,[4,*] and Klara Grantz Saskova[1,3,8,*]

SUMMARY

DDI2 is an aspartic protease that cleaves polyubiquitinated substrates. Upon proteotoxic stress, DDI2 activates the transcription factor TCF11/NRF1 (NFE2L1), crucial for maintaining proteostasis in mammalian cells, enabling the expression of rescue factors, including proteasome subunits. Here, we describe the consequences of DDI2 ablation *in vivo* and in cells. DDI2 knock-out (KO) in mice caused embryonic lethality at E12.5 with severe developmental failure. Molecular characterization of embryos showed insufficient proteasome expression with proteotoxic stress, accumulation of high molecular weight ubiquitin conjugates and induction of the unfolded protein response (UPR) and cell death pathways. In *DDI2* surrogate KO cells, proteotoxic stress activated the integrated stress response (ISR) and induced a type I interferon (IFN) signature and IFN-induced proliferative signaling, possibly ensuring survival. These results indicate an important role for DDI2 in the cell-tissue proteostasis network and in maintaining a balanced immune response.

INTRODUCTION

The ubiquitin proteasome system (UPS) serves primarily to degrade most intracellular proteins. Regulatory, misfolded or damaged proteins are tagged with ubiquitin chains and targeted to the proteasome. The proteasome consists of the 20S proteolytic core complex containing active site β-subunits, and axially attached regulatory complexes for binding, deconjugating, unfolding, and translocating ubiquitin-modified substrates into the proteolytic 20S complex.[1]

By controlling the intracellular pool of regulators, proteasomes actively participate in the regulation of various signaling pathways, including mTOR, the unfolded protein response (UPR), the integrated stress response (ISR), and both innate and adaptive immune responses.[2–6] UPS maintains proteostasis, ensuring cell integrity, viability, and function. Proteotoxic stress can be countered by halting protein translation or by boosting protein quality control and degradation machineries, including sets of ubiquitin-conjugation and deconjugation factors or alternative proteasome isoforms. Consequently, ISR and UPR pathways serve as hubs for integrated cellular response to proteotoxic stress in order to determine cell fate.[7–10] Both play regulatory roles beyond protein quality control, impacting inflammation and metabolism. Central to that is eIF2α phosphorylation by stress sensors like the kinases PERK, PKR, and GCN2, resulting in suppression of protein translation to decrease the protein load.[11,12]

The NGLY1-p97/VCP-DDI2-TCF11/NRF1 axis represents another important rescue mechanism to combat proteotoxic stress with implications for cancer treatment.[13–16] The transcription factor TCF11/NRF1 encoded by *NFE2L1* gene (NFE2-related factor 1) is a key regulator of proteasome formation in a time and concentration-dependent adaptive response.[13,17,18] Under normal conditions, the ER-tethered TCF11/NRF1 is permanently targeted for ER-associated degradation (ERAD) involving the HRD1 E3 ubiquitin ligase and the AAA-ATPase p97/VCP. During proteotoxic stress, TCF11/NRF1 is extracted by p97/VCP, deglycosylated by NGLY1 and cleaved by the aspartic protease DDI2, enabling its nuclear translocation.[19–21] This is crucial for the induction of rescue genes, including new proteasome subunits and other UPS-related factors.[13] DDI2 delays the degradation of TCF11/NRF1, by promoting its activation and protecting TCF11/NRF1 from ERAD.[14,22]

Recent pioneering work shows that during proteasome impairment or oxidative stress, the activation of TCF11/NRF1 transcriptional pathways results in the induction of downstream events associated with UPR and ISR, including induced transcription of ER chaperones, and

[1]Institute of Organic Chemistry and Biochemistry of the Academy of Sciences of the Czech Republic, Flemingovo n. 2, 166 10 Prague, Czech Republic
[2]First Faculty of Medicine, Charles University in Prague, Katerinska 32, 121 08 Prague, Czech Republic
[3]Department of Genetics and Microbiology, Faculty of Science, Charles University, BIOCEV, 25242 Vestec, Czech Republic
[4]Institute of Medical Biochemistry and Molecular Biology, Universitätsmedizin Greifswald, Ferdinand-Sauerbruch-Straße, Klinikum DZ 7, 17475 Greifswald, Germany
[5]Department of Functional Genomics, Universitätsmedizin Greifswald, Felix-Hausdorff-Str. 8, 17475 Greifswald, Germany
[6]Institute of Molecular Genetics of the Czech Academy of Sciences, Czech Centre for Phenogenomics and Laboratory of Transgenic Models of Diseases, BIOCEV, 25242 Vestec, Czech Republic
[7]These authors contributed equally
[8]Lead contact
*Correspondence: elke.krueger@uni-greifswald.de (E.K.), saskova2@natur.cuni.cz (K.G.S.)
https://doi.org/10.1016/j.isci.2024.110893

processing of XBP-1.[23,24] Interestingly, a rare homozygous deep intronic mutation in the *PSMC3* gene, encoding proteasome ATPase subunit RPT5, was shown to induce proteotoxic stress in patient's cells. However, the TCF11/NRF1 transcriptional pathway was unable to promote proteasome recovery, resulting in a fulminant proteotoxic crisis.[25] Cellular responses to proteasome impairment include additionally the dysregulation of type I interferon (IFN) signaling by mechanisms involving UPR and ISR components.[23,24,26–28]

DDI2 has a retroviral protease-like domain (RVP) similar to HIV protease. Structural analysis confirmed its conserved fold characterized by flexible flaps covering a large active site cavity.[20] The N-terminal ubiquitin-like domain and the C-terminal ubiquitin interaction motif weakly but specifically bind ubiquitin.[20] The helical domain of DDI2 (HDD) may participate in substrate recognition, supported by findings that Ddi1p and DDI2 are required to remove RPT2 from stalled replisomes and that HDD from yeast Ddi1 is involved in replication stress.[20,29–31] Importantly, yeast Ddi1 and mammalian DDI2 proteins have been shown to be polyubiquitin-dependent endoproteases[32–34] with TCF11/NRF1 and NRF3 as specific substrates.[19,35,36] Very recently it was shown that DDI2-mediated cleavage of angiomotin is required for retinal angiogenesis.[37]

Although some aspects of mammalian DDI2 functions are understood, its physiological role and functional complexity *in vivo* remain unclear. Applying conditions of DDI2 deficiency to cells and mouse models, we provide evidence that DDI2 is essential for physiological growth, development, and proteostasis maintenance. Proteotoxic stress and concomitant activation of UPR and ISR caused embryonic death in mouse models, but ultimately promoted the induction of type I IFN-stimulated genes that allowed proliferation signaling and survival of DDI2-knock out (KO) in cells.

RESULTS

DDI2 deficiency in mice results in mid-gestation embryonic lethality

To understand the biological role of DDI2 in a complex system, we generated two mouse strains in which DDI2 function was switched off either by knocking out *Ddi2* or replacing it with a *Ddi2* protease-defective allele. The complete KO strain *C57BL/6NCrl-Ddi2*$^{tm1b(EUCOMM)Hmgu}$*/Ph*, in text referred to as *Ddi2*^{KO} (genotypes *Ddi2*$^{+/+}$, *Ddi2*$^{+/-}$ and *Ddi2*$^{-/-}$), lacks the critical exon 2 and contains a *LacZ* reporter gene. The second strain was designed to disrupt two critical functions of the DDI2 protease domain – catalytic activity and dimerization. This *C57Bl/6NCrl-Ddi2*^{em1}*/Ph* strain, in text further referred to as *Ddi2*^{ex6} (genotypes *Ddi2*$^{ex6+/+}$, *Ddi2*$^{ex6+/-}$, and *Ddi2*$^{ex6-/-}$), was generated by TALEN-mediated excision of exon 6 of the *Ddi2* gene in a *C57Bl/6NCrl* background, resulting in ablation of the DDI2 protease domain (Δ254-296) (Figure 1A). Genomic DNA from *Ddi2*^{ex6} F1-generation animals used to establish colonies was screened for off-target modifications at 12 probable sites, with no detected off-target alterations. Systemic phenotyping of adult mice of both *Ddi2*-altered strains, aged 9–16 weeks, showed that heterozygous *Ddi2*$^{+/-}$ and *Ddi2*$^{ex6+/-}$ mice are viable, fertile and without a clear distinct phenotype. However, in both strains, homozygous mutants exhibited embryonic lethality in the mid-gestation period.

The *Ddi2*$^{-/-}$ embryos died between stages E11.5 and E14.5, with only one highly developmentally delayed survivor detected at stage E14.5 of the 48 total embryos harvested at this stage (Figures 1B, S1A, and S1B). At developmental stage E9.5, no differences were observed between the *Ddi2*$^{ex6-/-}$ and *Ddi2*$^{ex6+/+}$ littermate embryos (Figure 1C).

Although *Ddi2*$^{ex6-/-}$ embryos phenomimic the *Ddi2*^{KO} embryos in the onset of the lethal period at E11.5, the first signs of severe growth retardation were observed at E10.5 only in *Ddi2*$^{ex6-/-}$ embryos (Figure 1D). A significant alteration in both strains appeared at stage E11.5, in which half of the embryos were dead and the rest showed obvious growth retardation (Figure 1E). We were unable to detect living *Ddi2*$^{ex6-/-}$ embryos at E12.5, suggesting an earlier appearance of developmental defects and a narrower window of lethality in the *Ddi2*$^{ex6-/-}$ embryos compared to *Ddi2*$^{-/-}$ embryos.

Next, we analyzed the expression pattern of both the *Ddi2*^{WT} and *Ddi2*^{ex6} versions of *Ddi2* mRNA in *Ddi2*^{ex6} at E10.5. While qRT-PCR experiments confirmed the expression of *Ddi2*^{ex6} mRNA in embryonic samples of both the *Ddi2*$^{ex6+/-}$ and the *Ddi2*$^{ex6-/-}$ genotypes (Figure 1F), the DDI2^{ex6} protein was scarcely detectable in embryonic tissue lysates in immunoblot experiments (Figure 1A). The folding and stability of the recombinant DDI2^{ex6} protein was investigated using nuclear magnetic resonance (NMR) and differential scanning fluorimetry (DSF). The 1D NMR spectrum of the DDI2^{ex6} protein showed protein signals of acquired secondary structures, however, the melting temperature of DDI2^{ex6} could not be measured by DSF, although that of DDI2^{WT} could (Figures S1C and S1D). Furthermore, levels of expression of the recombinant DDI2^{ex6} protein in a model HEK293-TetOff-A cell line were lower at identical time points after transfection when compared to the DDI2^{WT} protein (Figure S1E). Together, these results indicate that *in vivo*, the DDI2^{ex6} protein likely undergoes rapid degradation.

The severe growth retardation of both *Ddi2*^{KO} and *Ddi2*^{ex6} strains suggests a systemic effect of *Ddi2* dysfunction on critical developmental components. To map the expression of *Ddi2* during embryonic development, *LacZ* reporter knock-in in *Ddi2*$^{+/-}$ mice was combined with *Ddi2 in situ* hybridization. *Ddi2* expression at E9.5 was detected in embryo regions with the most dynamic development at this stage, including orofacial processes (maxilla, mandible), otic placode, dorsal aorta, and tail bud (Figure 1G). *Ddi2* mRNA levels were twice higher at this stage compared to E10.5 and E11.5 (Figure S1F). The expression of *Ddi2* later expanded into most other tissues and was also visible in placenta (Figure S1G) and in developing heart (Figure S1H). Sagittal sections of the head at stage E14.5 revealed a localization in a specific layer of the cortex (forebrain and trigeminal ganglion) in the ectoderm and in mesodermal tissue, such as the cranium (Figure S1H). The broad expression of *Ddi2* suggests that *Ddi2* is an essential gene for systemic physiological functions during embryonic development.

In adult mice, the Ddi2 expression belongs to organs developed from the three germ layers (analysis by LacZ expression). Ddi2 expression in ectodermal and mesodermal tissue was mapped in the reproductive system of both sexes, the lungs, and the kidneys (Figure S2) as well as in the gray matter of brain, in peripheral neurons, in the epidermis, and in a number of glands of the main ectodermal tissue (Figure S3). Notably, *Ddi2* is also expressed in the bone marrow and the endothelial layer of vessels, serving as a key criterion for selecting an endothelial

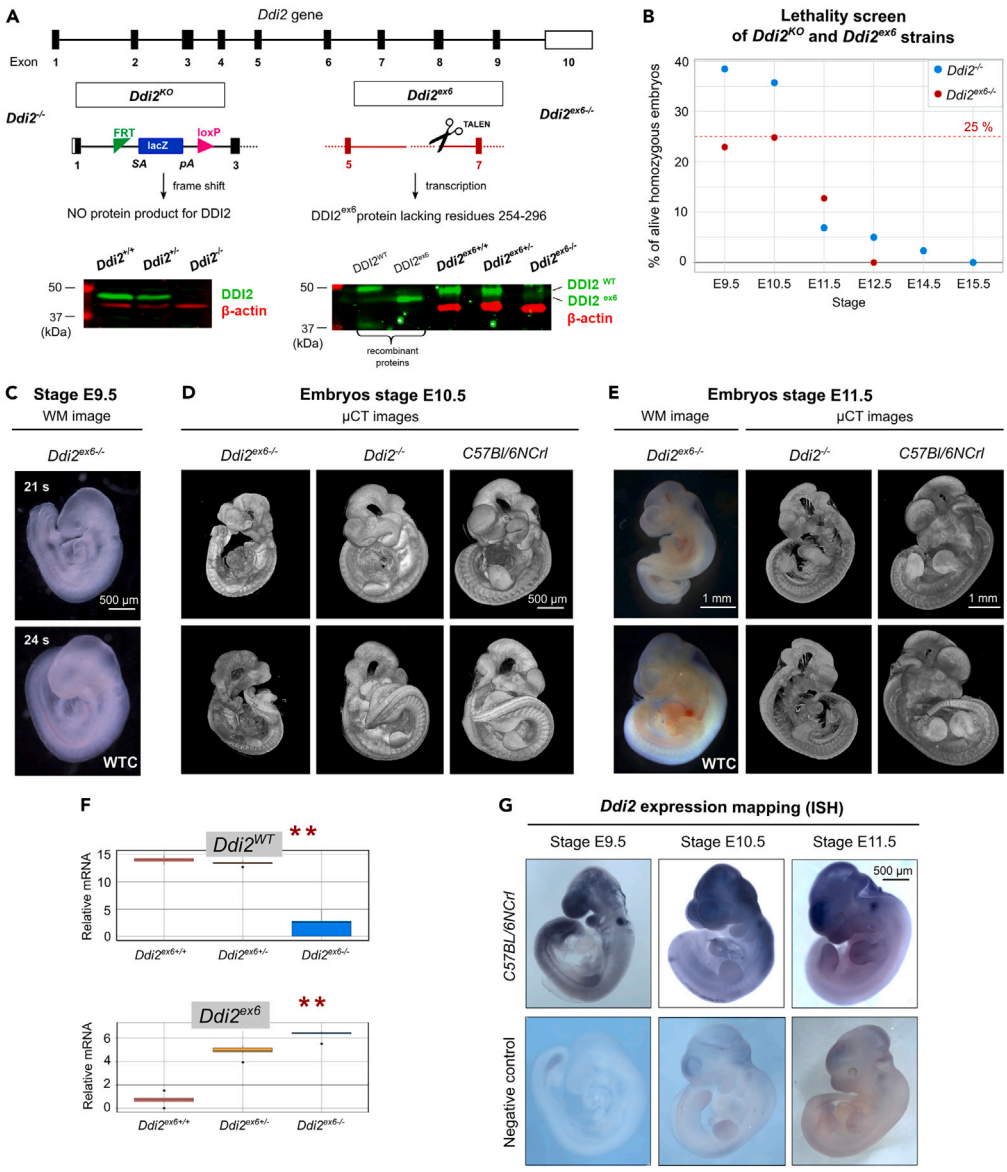

Figure 1. DDI2 dysfunction in mice results in mid-gestation embryonic lethality

(A) Scheme of *Ddi2* gene alternations: left—*Ddi2*^{KO} carries a *lacZ* reporter gene-tagged allele lacking the critical exon 2 representing complete knock-out model, right—*Ddi2*^{ex6} carries deletion of exon 6 generated by TALEN-mediated excision resulting in protease inactivation. Immunoblot of DDI2 protein expression in E10.5 embryo lysates: left—*Ddi2*^{KO}; right—*Ddi2*^{ex6} (lane 1 and 2—DDI2^{WT} and DDI2^{ex6} recombinant proteins). β-actin used as a loading control.

(B) Lethality screening of *Ddi2*^{KO} and *Ddi2*^{ex6} mouse strains, the plot shows percentage of living homozygous embryos. *Ddi2*$^{ex6-/-}$ embryos exhibit a narrower window of lethality compared to *Ddi2*$^{-/-}$ embryos. Detailed distributions of genotypes per stage and per group of living and dead embryos are shown in Figures S1A and S1B.

(C) No differences were observed between *Ddi2*$^{ex6-/-}$ (top) and *Ddi2*$^{ex6+/+}$ (bottom) littermate embryos at developmental stage E9.5. The number of somites is stated in each image.

(D) Phenotyping of stage E10.5 embryos. Comparison of µCT scans of *Ddi2*$^{ex6-/-}$ (left), *Ddi2*$^{-/-}$ (middle), and control *C57BL/6NCrl* (right) embryos using surface rendering representation. The 2D images of the 3D µCT scans are shown from both sides.

(E) Phenotyping of stage E11.5 embryos. Whole mount image of *Ddi2*$^{ex6-/-}$ embryo (top left) compared to its wild-type littermate (bottom left). Surface rendering of *Ddi2*$^{-/-}$ and *C57BL/6NCrl* control embryo µCT scans (middle and right, respectively). The 2D images of the 3D µCT scans are shown from both sides. WTC—wild-type control.

(F) Boxplots showing relative expression of *Ddi2*^{WT} (top) and truncated *Ddi2*^{ex6} (bottom) forms of mRNA expressed in *Ddi2*^{ex6} E10.5 stage embryos (*Ddi2*$^{ex6+/+}$—red, *Ddi2*$^{ex6+/-}$—yellow, *Ddi2*$^{ex6-/-}$—blue; $n = 7$). Relative expression was normalized to the housekeeping genes *Tbp* and *H2afz* with applied ANOVA statistical analysis (**). The error bars denote SD.

(G) *Ddi2* expression analysis using RNA *in situ* hybridization of *C57BL/6NCrl* embryos. Three developmental stages at the beginning of the onset of developmental failure in the *Ddi2* knock-out model strains are shown.

cell line as appropriate human cell line model for future experiments *in vitro*. Control expression of *Ddi2*^{4ex6} gene for all three developmental stages is given in Figure S3D. As *Ddi1* is a single-intron homolog of *Ddi2*, supplementing the role of Ddi2 in DNA damage response, we also monitored the expression *Ddi1* during mid-gestation embryonic development upon *Ddi2* depletion (Figure S3E). As we did not observe an increase in *Ddi1* mRNA, and considering that the expression patterns of the two homologs are distinct, we concluded that they cannot compensate for each other.

Ddi2 dysfunction results in unresolved proteotoxic stress, leading to developmental failure and premature death

To examine whether DDI2 dysfunction in mouse alters downstream UPR/ISR signaling we performed a qRT-PCR analysis of *Ddi2*^{ex6} embryos harvested at stages before the onset of lethality and analyzed the mRNA levels of characteristic UPR genes (Figure 2A). The expression of *Atf4* and *Chop* mRNA as well as *Herpud1*, a gene upregulated with ER stress, was significantly increased in *Ddi2*$^{ex6-/-}$ embryos in stages E10.5 and E11.5 compared to *Ddi2*$^{ex6+/+}$, and statistically significant throughout the three embryonic stages. Interestingly, increased expression of *Xpc* and *Bcl2* points to the activation of DNA-damage and apoptotic pathways.

Western blot analysis of embryo lysates (at E10.5) revealed activation of the PERK pathway of the UPR. We detected increased autophosphorylation of PERK (P-PERK) in *Ddi2*$^{ex6-/-}$ embryos compared to *Ddi2*$^{ex6+/+}$ and subsequent increased eIF2α phosphorylation (P-eIF2α), whereas PKR remained unchanged and phospho-PKR (P-PKR) could not be detected excluding involvement of PKR in downstream effects. PERK activation resulted in an increase in ATF4 (Figure 2B). ATF4 in turn transactivates CHOP (Figure 2A), indicating that cell death was induced in these stages of embryonic development.[10] This was confirmed by an increase of cleaved caspase 3. In addition, other regulatory pathways appeared to be altered by Ddi2 dysfunction, such as activated cell-cycle arrest (p21) and DNA damage response (γH2AX) or down-regulation of cell cycle progression (P-Rb and cyclin E1) (Figure 2C).

In line with the aforementioned stress-coping pathways and effects of DDI2 deficiency in cells,[33] the accumulated ubiquitin conjugates in *Ddi2*$^{ex6-/-}$ embryos notably exhibited higher molecular weight (Figure 2D). To this end, DDI2 dysfunction in mice caused severe proteotoxic stress characterized by upregulation of the UPR and cell death pathways.

DDI2 dysfunction in endothelial cells and mice alters UPS genes expression

To investigate the effect of DDI2 dysfunction at the molecular level, we implemented a proteomic approach to identify the most affected pathways in *DDI2* KO EAhy926 cells[22] and EAhy926 parental cells. Mass spectrometry analysis identified 2929 proteins, out of which 282 proteins fulfilled the parameters for further analysis of their functional categories. Based on the search using the reactome database, we observed alterations in proteins involved in protein metabolism, cell stress response, and pathways of the immune system (Figure 3A). The heatmap of the protein metabolism pathway (Figure 3B) visualized altered levels of several members of the proteostasis network, such as E3 ubiquitin ligases, deubiquitinating enzymes, proteasome subunits, ribosome proteins, and amino-acyl-tRNA synthetases.

DDI2 has been identified as the major protease responsible for activating the cleavage of the transcription factor TCF11/NRF1[14,19,33] modulating expression of a subset of UPS factors and proteasome subunits.[13,18] Therefore, we decided to explore how DDI2 KO cells cope with proteotoxic stress. We treated *DDI2* KO EAhy926 cells and EAhy926 parental cells with bortezomib (BTZ), an inhibitor of the proteasome chymotrypsin-like activity.[38] To address the importance of DDI2 in proteasome gene expression (Figure 3C), we determined relative levels of messenger RNA (mRNA) of representative core subunits (*PSMA2*/α2, *PSMB6*/β1) and regulatory proteasome complexes (*PSMC4*/RPT3, *PSME2*/PA28β) by qRT-PCR. Relative mRNA levels of *NFE2L1* in *DDI2* KO cells increased modestly compared to parental cells after BTZ treatment.

As expected and consistent with previous data,[13,14,18,19] the expression of proteasomal subunits (except PSME2/PA28β) increased in EAhy926 parental cells upon proteasome inhibition, although to different extents. *PSMC4* expression was impaired in *DDI2* KO cells compared to parental cells upon inhibition with BTZ. *PSMA2* upregulation was not affected in the background of *DDI2* KO, suggesting that transcription factors such as NRF2 can transactivate the *PSMA2* gene in this context. Interestingly, *PSME2* was modestly upregulated in *DDI2* KO cells compared to BTZ treated parental cells, indicating that *DDI2* KO cells upregulate alternative proteasome regulators (see also Figure 5).

Next, we aimed to analyze the *Ddi2*^{ex6} strain embryos for expression of *Nfe2l1* (NRF1) target genes and other UPS factors by qRT-PCR analysis harvested at stages before onset of lethality. While proteasome subunit genes (*Psma4*, *Psma6*, and *Psmb6*) did not show striking differences in expression, *Ngly1* showed a significant 2-fold increase at stage E10.5 compared to *Ddi2*$^{ex6+/+}$. The expression of the shuttling proteins *Rad23a* and *Rad23b* increased significantly after depletion of DDI2 function in embryos at stage E10.5 compared to *Ddi2*$^{ex6+/+}$ with significance throughout the three embryonic stages (Figure 3D).

DDI2 dysfunction leads to altered proteasome composition and activity

To verify our conclusions from the mRNA expression experiments with respect to proteasome expression, composition, and activity, we studied the effect of DDI2 dysfunction in EAhy926 *DDI2* KO cells and *Ddi2*^{ex6} embryos by native PAGE. The abundance of proteasome complexes in parental EAhy926 and *DDI2* KO cells (2 different clones, #4 and #17) was analyzed in BTZ-treated cells compared to untreated controls (Figure 4A).

Immunoblots of native PAGE gels, stained for α6 and RPN5 subunits, revealed significant elevated levels of 30S proteasomes in parental cells after BTZ treatment due to proteasome upregulation by TCF11/NRF1. *DDI2* KO cells failed to upregulate proteasomes in response to proteasome inhibition and displayed decreased proteasome levels with and without BTZ treatment. The decreased proportion of free 19S

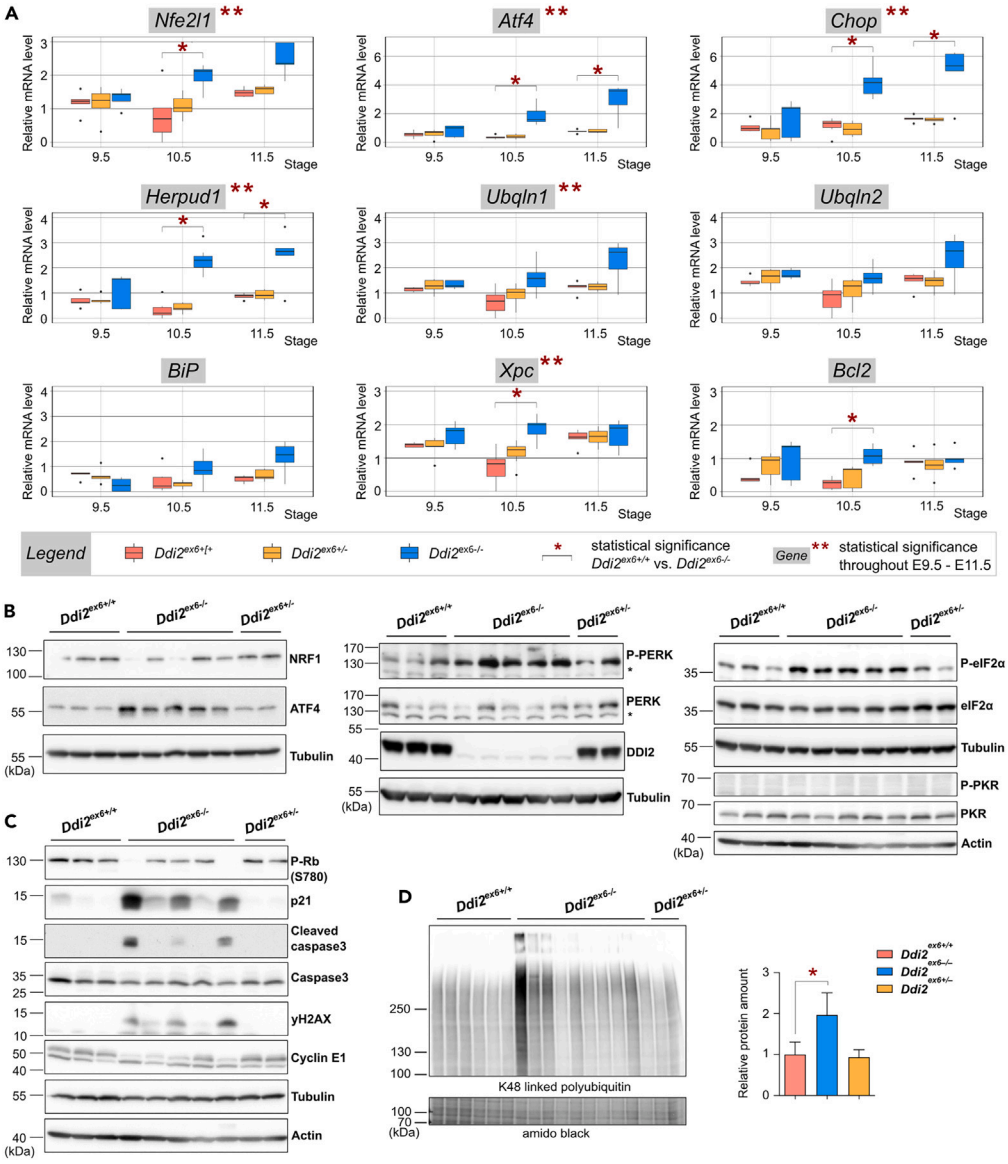

Figure 2. DDI2 dysfunction in mouse embryos leads to systematic breakdown causing premature death

(A) RT-qPCR analysis of UPR involved genes in *Ddi2*^{ex6} embryos among stages prior to the onset of lethality. Legend: *Ddi2*$^{ex6+/+}$ —red, *Ddi2*$^{ex6+/-}$—yellow, *Ddi2*$^{ex6-/-}$—blue; E9.5 (n = 5), E10.5 (n = 7), E11.5 (n = 5). The relative expression was normalized to the housekeeping genes *Tbp* and *H2afz*. Statistical significance was calculated for each gene throughout the three stages of embryonal development using ANOVA analysis (**) or using a linear mixed-effects model (LMM) for the comparison of gene expression between wild-type and homozygous embryos at each stage of development (*). Both analyses were subjected to Bonferroni correction; boxplots with SD.

(B) Representative immunoblots of key markers of the UPR and ISR pathways (NRF1, ATF4, P-PERK, PERK, DDI2, P-eIF2α, eIF2α, P-PKR, and PKR) in tissue lysates of *Ddi2*$^{ex6+/+}$ (n = 6), *Ddi2*$^{ex6-/-}$ (n = 10), and *Ddi2*$^{ex6+/-}$ (n = 3) embryos. Tubulin and actin were used as loading controls. The black asterisks denote nonspecific bands.

(C) Representative immunoblots of DNA-damage markers (γH2AX), cell cycle (P-Rb, cyclin E1, p21) and apoptosis markers (cleaved caspase 3, caspase 3) in tissue lysates of *Ddi2*$^{ex6+/+}$ (n = 6), *Ddi2*$^{ex6-/-}$ (n = 10) and *Ddi2*$^{ex6+/-}$ (n = 3) embryos. Tubulin and actin were used as loading controls.

(D) Western blot analysis of the insoluble fraction of *Ddi2*$^{ex6+/+}$ (n = 6, red), *Ddi2*$^{ex6-/-}$ (n = 10, blue) and *Ddi2*$^{ex6+/-}$ (n = 2, yellow) embryo tissue lysates show accumulation of polyubiquitinated proteins of higher molecular weight. The membrane was probed with an anti-K48 linked polyubiquitin antibody, and the expression of ubiquitin conjugates with a molecular weight above 250 kDa was densitometrically quantified and normalized to the Amido Black loading control. The outlier in lane 7 was excluded from the calculation. Statistical significance was determined between *Ddi2*$^{ex6+/+}$ and *Ddi2*$^{ex6-/-}$ using Mann-Whitney-test (*p value $\leq$0.05; bar with mean ± SD).

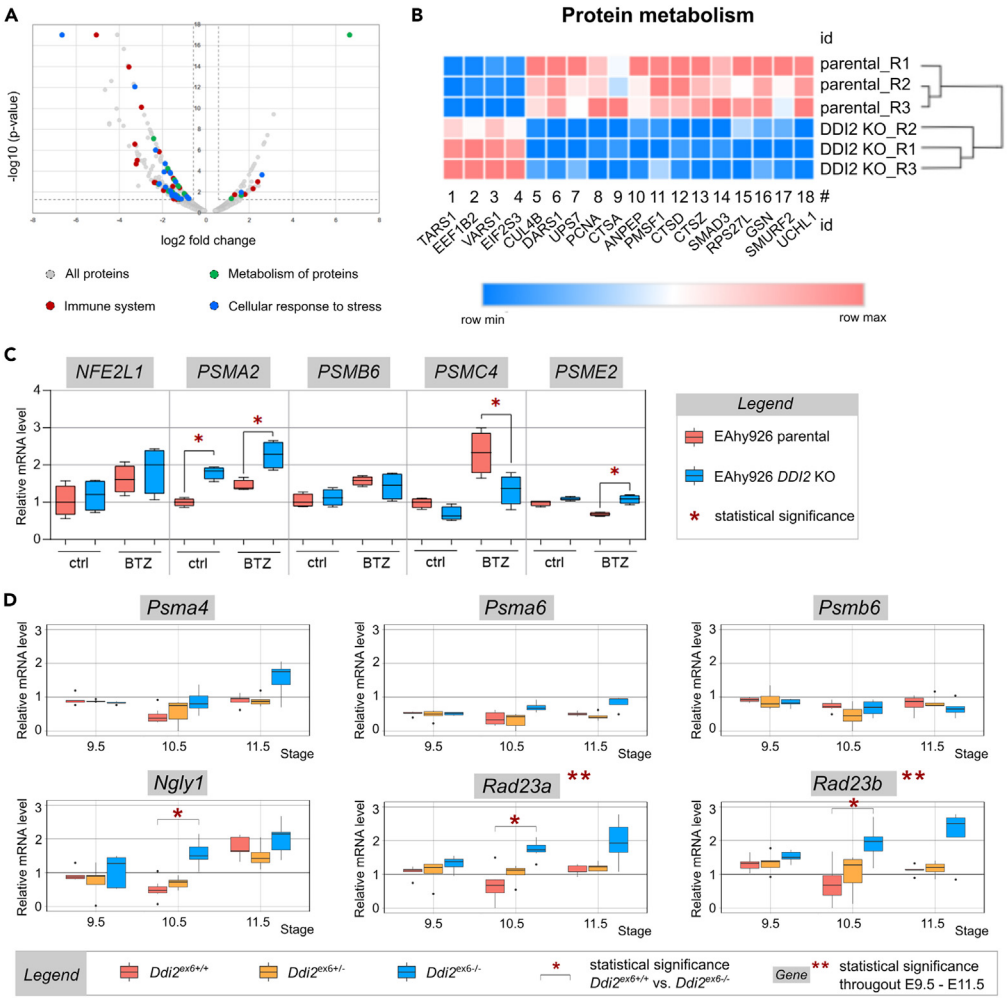

Figure 3. DDI2 dysfunction in mice and endothelial cells alters UPS gene expression and abundance of proteins involved in proteostasis

(A) Volcano plot of differentially abundant proteins in DDI2 KO cells compared to parental cells. Member proteins of over-represented pathways based on reactome analysis are highlighted. Quantitative analysis based on 3 biological replicates. Pathways enrichment analysis was performed using a list of 282 differentially abundant proteins with the Reactome database vs.79.

(B) Heatmap showing differences in the protein metabolism network from the top identified and differentially abundant proteins with more than 1.5-fold difference between DDI2 KO cells (clone 17) and the parental cell line (n = 3).

(C) RT-qPCR analysis of mRNA of *NFE2L1* (TCF11/NRF1) and proteasomal subunits *PSMA2* (α2), *PSMB6* (β1), *PSMC4* (RPT3), and *PSME2* (PA28β) in EAhy926 parental cells (red) and *DDI2* KO (blue) cells. Cells were treated with 50 nM BTZ for 8 h. Messenger RNA levels were normalized to *RPLP0*. two-way ANOVA was used for statistical calculation (n = 4; *p value $\leq$0.05; box and whiskers with min to max).

(D) qRT-PCR analysis of NRF1-regulated genes in the UPS pathway in *Ddi2*^{ex6} embryos in stages prior to the onset of lethality. Legend: *Ddi2*$^{ex6+/+}$ —red, *Ddi2*$^{ex6+/-}$—yellow, *Ddi2*$^{ex6-/-}$—blue; E9.5 (n = 5), E10.5 (n = 7), E11.5 (n = 5). Relative expression of genes was normalized to *Tbp* and *H2afz* housekeeping genes. Statistical significance was calculated for each gene at all three developmental stages with application of ANOVA statistical analysis (**) or using a linear mixed-effects model (LMM) for comparison of gene expression between wild-type and homozygous embryos at each developmental stage (*p value $\leq$0.05; boxplots with SD). Both analyses were subjected to Bonferroni correction.

particles (see RPN5 staining) suggested a greater association of 19S regulatory particles with 20S core proteasomes to form single- or double-capped proteasome complexes to enhance proteolytic capacity under these conditions.[39]

Both, the immunoproteasome subunit β5i/LMP7 and PA28β, are expressed at higher levels in the DDI2 KO cells (Figure 4B).[40] *DDI2* KO cells most likely compensate for impaired proteasome formation by inducing immuno- and hybrid proteasomes, defined proteasome isoforms.[41]

As expected, chymotrypsin-like (CT-L) activity was almost completely eliminated in parental cells treated with BTZ. Surprisingly, clone #17 of *DDI2* KO cells showed higher CT-L activity under untreated conditions and even maintained modest CT-L activity after BTZ treatment, especially of the 20S proteasome (Figure 4C). This is due to the increased recruitment of PA28/11S (Figure 4B), which is known to activate the peptide hydrolysis activity of 20S proteasome complexes.[42] This phenomenon was less pronounced in clone #4 of *DDI2* KO cells.

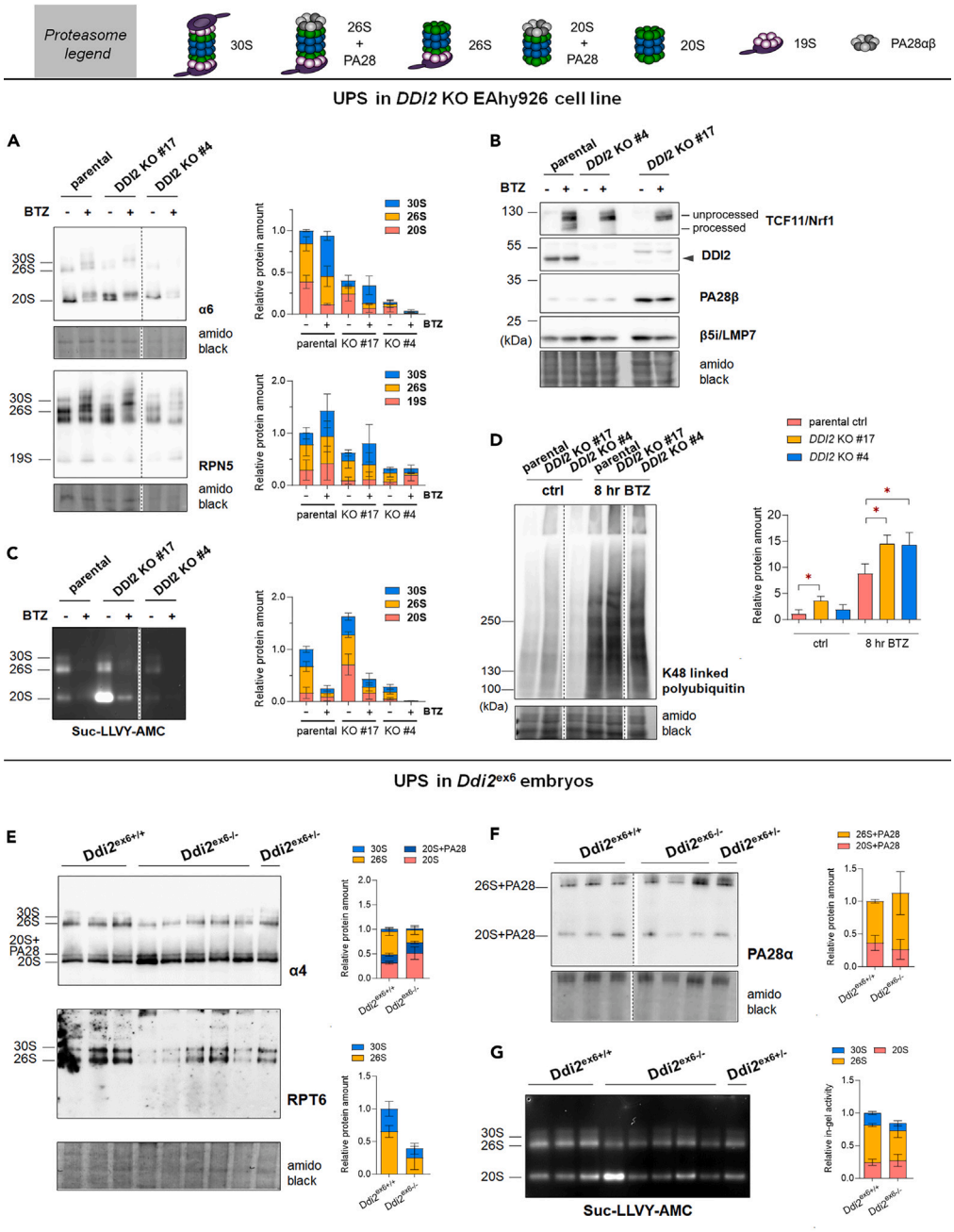

Figure 4. DDI2 dysfunction alters proteasome composition and activity, leading to accumulation of high molecular weight polyubiquitinated proteins

Proteasomal complexes analyzed is schematically illustrated in the legend. Amido Black staining served as loading control. Vertical dashed line depicts border between two areas from one western blot membrane. Statistical calculation of the *p* value was performed using two-way ANOVA with Šídák's multiple comparisons test except 4D (unpaired t-test). Summarized data were given in Table S7. The native tissue lysates of Ddi2ex6$^{+/-}$ embryos were given exemplary and not quantified. (A) Immunoblots after native page analyzing expression of proteasomal subunits α6 and RPN5 in native cell lysates of parental EAhy926 and *DDI2* KO cells (clones #4 and #17) treated with 50 nM BTZ for 8 h compared to non-treated controls (n = 3, 20 μg of total protein/lane; quantification given by bar with mean ± SD). (B) Immunoblots of TCF11, DDI2, PA28β, and β5i/LMP7 in whole cell extracts of EAhy926 parental and *DDI2* KO cells (clones #4 and #17) treated with 50 nM BTZ for 8 h compared to non-treated controls (n = 3, 25 μg of total protein/lane).

(C) Chymotrypsin-like activity of native cell lysates of EAhy926 parental and *DDI2* KO cells treated with 50 nM BTZ for 8 h compared to non-treated controls (n = 3; quantification given by bar with mean ± SD) was measured in a gel-based assay with the fluorogenic substrate Suc-LLVY-AMC. Loading control was the same as for α6 immunoblot.

Figure 4. *Continued*

(D) Immunoblots for K-48 linked polyubiquitin of whole cell extracts of EAhy926 parental (red) and *DDI2* KO clone #17 (yellow) and clone #4 (blue) cells treated with 50 nM BTZ for 8 h compared to non-treated controls. The statistical significance was calculated using the unpaired two-sided t-test (*p value $\leq$0.05, n = 3; bar with mean ± SD).

(E and F) Representative immunoblots of native tissue lysates (15 μg of total protein/lane; quantification given by bar with mean ± SD) of $Ddi2^{ex6+/+}$ (n = 3), $Ddi2^{ex6-/-}$ (n = 5) and $Ddi2^{ex6+/-}$ (n = 1) embryos probed for proteasomal subunits α4, RPT6 and PA28α.

(G) Chymotrypsin-like activity of native tissue lysates of $Ddi2^{ex6+/+}$ (n = 3), $Ddi2^{ex6-/-}$ (n = 5), and $Ddi2^{ex6+/-}$ (n = 1) embryos was measured in gels based on the hydrolysis of the fluorogenic substrate Suc-LLVY-AMC. Loading control was the same as for α4 and RPT6; quantification given by bar with mean ± SD.

DDI2 KO cells were unable to fully compensate impaired proteasome activity. Analysis of ubiquitin conjugates by immunoblotting (Figures 4D and S4A) showed a significant enrichment of K48-linked polyubiquitylated proteins after BTZ treatment. Although EAhy926 parental cells accumulated high molecular weight polyubiquitylated proteins, especially detected in stacking gels, the effect was even more pronounced in the *DDI2* KO cells, as previously observed,[33] and could be rescued by the induced expression of the DDI2 wt protein (Figure S4B).

By staining proteasome complexes in embryos for the α4 and RPT6 subunits, we detected significantly lower levels of 26S proteasome in $Ddi2^{ex6-/-}$ compared to $Ddi2^{ex6+/+}$, while the levels of 20S proteasomes were increased (Figure 4E). The association of the alternative activator PA28/11S with 26S proteasomes was slightly, but not significantly increased (Figure 4F), although steady state expression of PA28 was decreased (Figure S4C). In agreement with the lower proteasome content in the $Ddi2^{ex6-/-}$ embryos compared to $Ddi2^{ex6+/+}$ embryos we detected a trend of decreased CT-L activity of 26S and 30S proteasomes (Figure 4G).

In conclusion, DDI2 deficiency in cells led to altered proteasome complexes with enhanced PA28/11S regulator levels and β5i/LMP7, resulting in increased peptide hydrolysis activity. In contrast, homozygous $Ddi2^{ex6-/-}$ embryos displayed a mild reduction in the CT-L activity accompanied by decreased levels of 26S/30S proteasomes.

DDI2 dysfunction activates NRF2

As proteotoxic stress by proteasome impairment is accompanied by oxidative stress,[18] and both NRF1 and NRF2 bind to antioxidant response elements (AREs) at their target promoters, we investigated the potential activation of the NRF2 pathway after DDI2 loss. Indeed, our pathway analysis of proteins involved in stress response in the cell model revealed NRF2-like signatures with upregulation of NRF2-target genes coding for proteins, such as thioredoxin, peroxiredoxins, and glutathione peroxidase 1 (Figure 5A). The expression of NRF2 after BTZ treatment was strongly induced and also more pronounced at an earlier time point in KO cells compared to parental cells (Figure 5B). Heme oxigenase (HO-1) expression, in turn, was more induced in parental cells compared to DDI2-deficient cells, indicating that HO-1 expression in endothelial cells is strictly dependent on TCF11/NRF1 and less on NRF2 (Figure 5C).

Nfe2l1 and *Nfe2l2* functions in oxidative stress response were previously shown to overlap during mouse early embryonic development.[43] Because the function of *Nfe2l1* is impaired in $Ddi2^{ex6}$ embryos, we next investigated whether the NRF2 pathway is activated in developmental stages prior to the onset of lethality. qRT-PCR analysis revealed a statistically significant increase in *Nfe2l2* mRNA expression in $Ddi2^{ex6-/-}$ embryos compared to $Ddi2^{ex6+/+}$ at E10.5 and E11.5, and also of several genes (*Gclm*, *Gss*, and *Hmox1*) involved in oxidative stress response (Figure 5D).[44]

Of these, *Hmox1* exhibits the largest increase in expression upon loss of *Ddi2* function at stages E10.5 and E11.5. Interestingly, the expression level of the second DDI2 substrate *Nfe2l3* mRNA did not change in embryonic stages prior to the onset of lethality (Figure S5A).[35,45] Expression of the mRNAs of NRF2 and heme oxygenase (HO-1) was correlated with a moderate increase in both proteins (Figure S5B).

DDI2 dysfunction induces downstream stress pathway markers

Stress pathway induction was investigated in *DDI2* KO cells compared to parental cells and in response to BTZ in time course experiments. As expected TCF11/NRF1 processing and nuclear translocation were almost completely impaired in *DDI2* KO cells (Figure S6E). This could be rescued by wild-type DDI2 expression, but not by inactive DDI2 protease variants (Figure S6F). However, a small amount of TCF11/NRF1 could still translocate into the nucleus after BTZ treatment, indicating an additional mechanism for TCF11/NRF1 activation (Figures 6A and 6B).[14]

We observed induction of *ATF4* mRNA in DDI2-deficient cells even under control conditions, which was more pronounced following treatment with BTZ (Figure S6A). Consistent with stronger induction of *ATF4* mRNA in *DDI2* KO cells, ATF4 protein levels also increased in the nucleus, and in the chromatin-associated fraction (Figure 6A). Furthermore, we detected increased protein levels of CHOP as a downstream target of ATF4 after BTZ treatment in DDI2-deficient cells (Figures 6D and S6C). Activation of ATF4 could be abolished by transfection of wild-type DDI2 into the KO cell line, indicating that ISR activation is caused by DDI2-deficiency (Figure S6G).

Following the idea of cellular responses to proteotoxic stress and the activation of eIF2α kinases by ISR,[9] increased levels of P-PKR were observed in both DDI2-deficient cells (Figure 6C). Consequently, parental and DDI2-deficient cells exhibited increased eIF2α phosphorylation in response to proteasome inhibition (Figure 6C). Increased phosphorylation of PERK and induction of the UPR (see Figure 2B) could not be observed in the DDI2 KO cell model (data not shown).

The transcription factors ATF4 and CHOP typically activated by P-eIF2α downstream events were strongly induced in response to BTZ (Figure 6D; S6B and S6D). Similar to DDI2-deficient mouse embryos showing cell death at stages with activated P-eIF2α downstream signaling (Figure 2), this activation was much more pronounced in DDI2-deficient cells compared to parental cells. Surprisingly, we could not detect

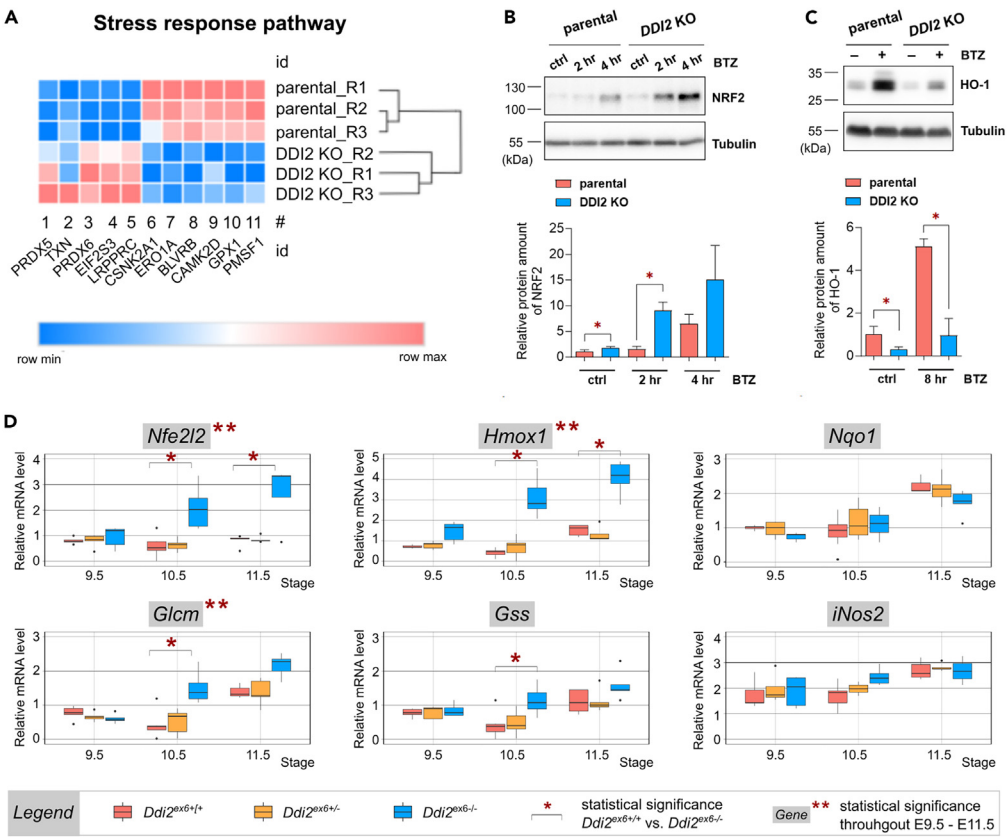

Figure 5. The NRF2 pathway is activated upon loss of DDI2

(A) Heatmap showing changes in the stress response pathway of the top identified and differentially abundant proteins with fold difference more than 1.5-fold between DDI2 KO cells (clone 17) and the parental cell line (n = 3).

(B) Immunoblots of NRF2 expression in whole cell extracts of the parental EAhy926 (red) and *DDI2* KO clone 17 (blue) treated with 50 nM BTZ for 2 and 4 h (NRF2 detection) in comparison to non-treated controls. Protein levels were quantified after normalization to the tubulin control signal. Statistical significance was determined using Mann-Whitney-test (n = 4; *p value $\leq$0.05; bar with mean $\pm$ SD).

(C) Immunoblots of HO-1 level in whole cell extracts of EAhy926 parental (red) and *DDI2* KO (blue) treated with 50 nM BTZ for 8 h in comparison to controls without treatment. Protein levels (n = 4) were quantified and statistically analyzed as in (B).

(D) RT-qPCR analysis of NRF1 and NRF2-regulated genes in *Ddi2*^{ex6} embryos in stages prior to the onset of lethality. Legend: *Ddi2*$^{ex6+/+}$—red, *Ddi2*$^{ex6+/-}$—yellow, *Ddi2*$^{ex6-/-}$—blue; E9.5 (n = 5), E10.5 (n = 7), E11.5 (n = 5). Relative expression of genes was normalized to *Tbp* and *H2afz* housekeeping genes; outliers were omitted based on the Grubbs' test. Statistical significance was calculated either for each gene throughout all three developmental stages with application of ANOVA statistical analysis (**) or using a linear mixed-effects model (LMM) for comparison of gene expression between wild-type and homozygous embryos at each developmental stage (*). Both analyses were subjected to Bonferroni correction; boxplots with SD.

obvious signs of cell death during culture of DDI2-deficient cells. Analysis of molecular markers for cell proliferation did not show significant differences in the levels of cyclin E1, P-Rb, or induction of p21 compared to parental cells (Figure 6E). Staining of yH2Ax revealed signs of DNA-damage in DDI2 KO cells, as observed in the embryos. Furthermore, DDI2-deficient cells exhibited activation of MAP-kinase signaling, as shown by staining for p38 and JNK typically seen in response to cytokine signaling. In summary, these data suggest that DDI2-deficiency caused severe proteotoxic stress and chronic activation of the ISR pathway. Nonetheless, DDI2-deficient cells may survive by activating proliferation signaling.

DDI2 dysfunction causes type I interferon signaling

Permanent proteasome impairment induces type I IFN signaling.[24,46] Indeed, our pathway enrichment analysis of DDI2 KO cells revealed IFN-signaling as one of the most relevant pathways (Figure 7A).

In the canonical pathway of type I IFN signaling the signals are recognized by pattern recognition receptors (PRRs) of the cell autonomous innate immune response. PRRs activate autophosphorylation of TBK1/IKKε/DDX3 subsequently leading to phosphorylation of transcription factors IRF3/IRF7 and activation of IFNα and β, which may stimulate autocrine and paracrine activation of IFN stimulated genes (Figure 7B). Indeed, we observed in embryos an upregulation of phospho-TBK1 (P-TBK1), but no phosphorylation of STAT1 (Figure 7C). This indicates that the receptors detected danger signals and activated TBK1 without downstream induction of IFN production

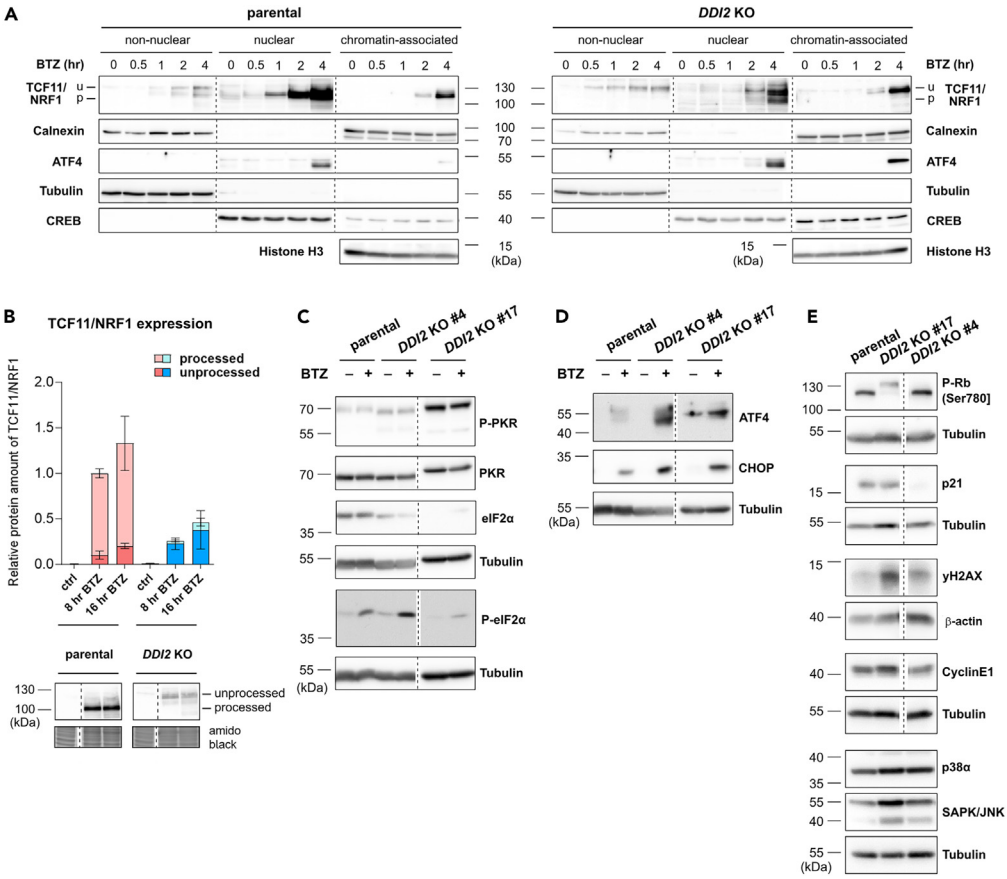

Figure 6. *DDI2* KO cells show reduced TCF11/NRF1 activation and increased downstream stress markers induction upon proteotoxic stress

(A) Analysis of TCF11/NRF1 and ATF4 levels in individual cellular fractions (nuclear, non-nuclear, and chromatin associated) of parental and *DDI2* KO EAhy926 cells (treatment with 50 nM BTZ for a 4-h time course, $n = 5$). Calnexin, tubulin, CREB, and histone H3 served as markers of individual fractions. u = unprocessed; p = processed.

(B) Immunoblots and quantification of TCF11/NRF1 protein abundance in whole cell extracts of parental EAhy926 (red) and *DDI2* KO (blue) treated with 50 nM BTZ for 8 and 16 h or without treatment. Quantification was performed upon normalization to an Amido Black loading control. Statistical calculation of the *p* value was performed using two-way ANOVA with Šídák's multiple comparisons test ($n = 3$; bar with mean ± SD). Summarized data were given in Table S7. For complete time course experiment see Figure S6C.

(C) Immunoblots of P-PKR, PKR, eIF2, and P-eIF2α in whole cell extracts from parental EAhy926 cells and clones #4 and #17 of *DDI2* KO cells, treated with 50 nM BTZ over a time course of 8 h ($n = 3$, 25 μg of total protein/lane). Vertical dashed lines depict border between two areas from one western blot membrane. The respective tubulin serves as loading control.

(D) Immunoblots of ATF4 and CHOP in whole cell extracts from parental EAhy926 cells and two clones of *DDI2* KO cells treated with 50 nM BTZ for 8 h ($n = 3$, 25 μg of total protein/lane). Vertical dashed lines depict border between two areas from one western blot membrane. Tubulin serves as loading control.

(E) Immunoblots of apoptosis and senescence markers in whole cell extracts from parental EAhy926 cells and two clones of *DDI2* KO cells ($n = 3$, 25 μg of total protein/lane). Vertical dashed lines depict border between two areas from one western blot membrane. The respective tubulin serves as loading control.

in embryos. Consequently, we did not detect significant expression of IFN-stimulated gene (ISG) in embryos deficient in DDI2 (Figure S7A).

In contrast, we observed strong IRF3 phosphorylation in DDI2-deficient cells, but did not detect high levels of P-TBK1, however, that of IKKε, which is known to act independently of TBK1 for downstream IFN-signaling. Interestingly, STAT1 expression was completely abolished in *DDI2* KO cells. Therefore, phospho-STAT1 (P-STAT1) was not detected (Figure 7D). The increased phosphorylation of IRF3 in *DDI2* KO cells was accompanied by chronic induction of specific ISGs along with *IFNB* (encoding IFN-β) (Figures 7E and S7C–S7E), a signature typical for interferonopathies.[47] Furthermore, cells deficient in DDI2 activated STAT3 phosphorylation instead of STAT1, indicating a non-canonical pathway for ISG induction (Figure 7D). In contrast, parental cells induced the classical pathway via P-TBK1 and P-STAT1 upon BTZ exposure, indicating activation of the cell autonomous innate immune signaling in response to proteasome impairment (Figures 7D and S7B).

From these data we concluded that DDI2-deficient embryos die from unresolved proteotoxic stress, whereas DDI2-deficient cells activate proliferation and type I IFN signaling.

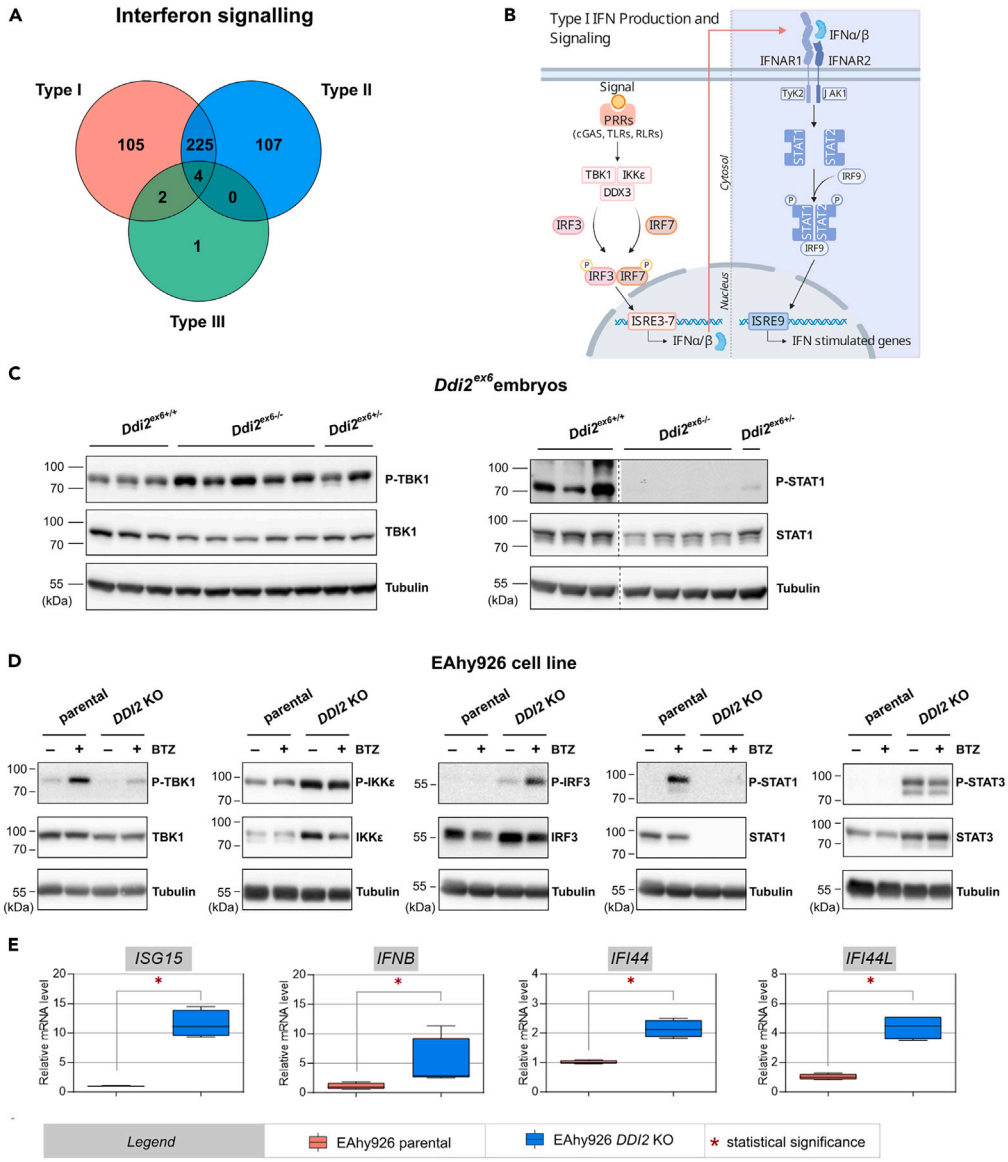

Figure 7. Depletion of DDI2 affects type I interferon signaling

(A) Venn diagram showing identification of an individual interferon regulated gene signature based on proteome data. The interferon assignment was divided into type I, type II, and type III. The numbers represent varying proteins, which are assigned differently to the types.

(B) Simplified scheme of one of the major type I interferon (IFN) production pathways and downstream signaling. The activation of various pattern recognition receptors (PRRs) initiates the activity of IκB kinase- (IKKε) and TANK-binding kinase-1 (TBK1) leading to DEAD box protein 3 (DDX3) mediated phosphorylation of the transcription factors IFN regulatory factor 3 (IRF3) and 7 (IRF7), serving as transcriptional activators of type I IFN. Upon binding of IFNα/β to the interferon alpha/beta receptor 1 and 2 (IFNAR1/2) the two Janus kinases (JAK and TYK2) bound to the receptor chains are activated. The signal transducer and activator of transcription 1 and 2 (STAT1/STAT2) are subsequently phosphorylated and released. These transcription factors form heterodimers and interact with IRF9. This complex migrates to the nucleus and induces transcription of IFN stimulated genes (ISGs). The scheme was created with BioRender.com.

(C) Representative immunoblots of differences in protein expression of P-TBK1, TBK1, P-STAT1, and STAT1 in *Ddi2*$^{ex6+/+}$ (n = 6), *Ddi2*$^{ex6-/-}$ (n = 10) and *Ddi2*$^{ex6+/-}$ (n = 3) embryos. Tubulin was used as a loading control. Vertical dashed lines depict border between two areas from one western blot membrane.

(D) Immunoblots of the protein expression of P-TBK1, TBK1, P-IKKε, IKKε, P-IRF3, IRF3, P-STAT1, STAT1, P-STAT3, and STAT3 in response to proteotoxic stress and under normal conditions. Expression was monitored in whole cell extracts of human EAhy926 parental cells and *DDI2* KO clone #17 cells treated with 50 nM BTZ for 8 h (n = 4, also see Figure S7F). Tubulin was used as a loading control.

(E) RT-qPCR expression analysis of key interferon stimulated genes *ISG15*, *IFNB*, *IFI44*, and *IFI44L* in human EAhy926 parental (red) and *DDI2* KO (blue, clone #17) cells (also see Figures S7C–S7E). Messenger RNA amounts were normalized to *RPLP0*. Statistical significance was calculated using Mann-Whitney test (n = 4, *p value ≤0.05; box and whiskers with min to max).

DISCUSSION

Proteostasis is affected throughout life by various processes, including development, differentiation, metabolic changes, immune responses, and aging.[48–50] Therefore, sophisticated mechanisms of tissue and cell-specific proteostatic pathways are crucial to mitigate protein aggregation, inclusion body formation, and ultimately cell death.

In this study, we demonstrated that *Ddi2* dysfunction in mice led to mid-late gestation embryonic lethality. DDI2 is an aspartic protease that proteolytically activates the highly polyubiquitylated transcription factor TCF11/NRF1 (NFE2L1), whose ubiquitination is catalyzed by different ubiquitin ligases.[18–20,32,33,51] The NGLY1-p97/VCP-DDI2-TCF11/NRF1 axis represents a major stress adaptation pathway activated upon proteasome impairment, preventing apoptosis, and promoting cell survival.[13,18,52] Although *Ngly1*,[53] *Nfe2l1*,[54] and proteasomal subunits[55] KOs in mice result in embryonic lethality, the importance of DDI2 within this pathway remained unclear. Both the complete KO and the protease-defective mouse models described here exhibit severe developmental failure. Detailed expression analysis revealed developmental defects mainly in tissues expressing *Ddi2*, particularly in the craniofacial region, limb buds, and heart (Figures 1, S1G, and S1H). Interestingly, NRF1-deficient mice had no obvious developmental defects prior to death, but suffered from anemia due to abnormal fetal liver erythropoiesis. However, at E10.5, both NRF1 and DDI2 null strains were smaller in comparison with wild type and heterozygous littermates.[54]

Analysis of potential transcription factor binding sites in the *DDI2* promoter region revealed hits for the FOX (forkhead box) and E2F families of transcription factors, indicating a dependence of DDI2 expression on cell cycle and developmental signaling pathways (GeneHancer database: http://genome.ucsc.edu/, unpublished results).[56] The expression of *Ddi2* around E10.5 closely resembles that of its substrate NRF1 (*Ne2lf1*).[57] Another identified DDI2 substrate, NRF3 (encoded by *Nfe2l3*),[35] remains unaffected by DDI2 deficiency during the mid- to late gestation period (Figure S5A). Earlier studies on *Ddi2* mRNA expression were confined to the mouse brain (mice from E13.5 up to 9 months) and *Ddi2* did not fluctuate. This differs from the dramatic increase in *Ddi1* mRNA at E16.5, which was attributed to a specific role for DDI1 in brain development.[58] While suggesting that DDI1 could compensate for DDI2 deficiency, observed in response to DNA damage,[30,59] we found no increase in *Ddi1* mRNA in the $Ddi2^{ex6-/-}$ embryos during the three critical developmental stages prior to death (Figure S3B). Moreover, the expression pattern of the two homologs is distinct.[58,60] Thus, the two DDI homologs cannot compensate for each other.

Interestingly, the expression patterns of several key members within this stress response axis (NRF1/NFE2L1, ATF4) closely resemble that of *Ddi2* from embryonic stages E9.5–E11.5, from which the last stage turned out to be the decision point for our DDI2-deficient mouse models (Figures 1B and 1G). Development of *Nrf1* null embryos was arrested a bit earlier before E7.5, as NRF1 is critical for mesoderm development.[61] This correlates with Ddi2 expression in all 3 germ layers. Note that while the upstream regulators (NGLY1, proteasome) belong to the essential genes that exhibit embryonic lethality,[53,54,62] KO mouse models of the downstream regulators such as ATF4, CHOP, STAT1, or STAT3 typically die during postnatal development.[63–65] In this context, it is important to note that proper stem cell function, signaling pathways of development and differentiation strongly rely on a functional UPS and require timely degradation of modulators to activate downstream transcription factors.[66–70] Therefore, developmental defects in DDI2-deficient mice are likely due to proteasome dysfunction (Figures 2 and 4), while compensatory mechanisms such as NRF2 or ISR induction (Figures 5 and 6), are insufficient to compensate for DDI2-deficiency. The strong induction of CHOP, caspase 3 cleavage, and decreased proliferation markers (pRB, cyclin E) in DDI2-deficient embryos at the time points of embryonic cell death (Figure 2) indicates induced cell death due to unresolved proteotoxic stress.

Upregulation of alternative proteasome isoforms and regulators such as immunoproteasomes and PA28/11S can help to maintain the proteostatic potential of cells and tissues during inflammation.[71,72] DDI2-deficient cells also induced such compensatory mechanisms (Figure 4). However, these proteins (typically IFN-regulated) were unable to resolve the proteotoxic crisis induced by DDI2 deficiency. Moreover, PA28 has been shown to be a transcriptional target of NRF2,[73] indicating that upregulation relies both on IFN signaling and NRF2.

Although knocking out key members of the NGLY1-p97/VCP-DDI2-TCF11/NRF1-proteasome pathway resulted in embryonic lethality, successful ablation in cells was demonstrated for DDI2,[14,19] NGLY1,[74] UBE4A,[51] and NRF1.[13,54] The difference between the embryonic lethality of $DDI2^{ex6-/-}$ and almost normally dividing *DDI2* KO cells is intriguing. In contrast to DDI2-deficient embryos with UPR and cell death induction, we observed ISR activation by PKR, but only moderate levels of phosphorylated eIF2α in DDI2-deficient cells (Figure 6C). The eIF2α phosphorylation and dephosphorylation cycle is crucial for promoting translational recovery and survival after stress.[75–77] suggesting that dephosphorylation of eIF2α may counter translational arrest to produce IFN-β as shown in other conditions.[78]

Proteasome impairment by pharmacological inhibition or by loss of function mutations in genes encoding proteasomal subunits but also NGLY1 impairment induce dysregulation of type I IFN signaling.[24,27,46,79,80].[74] Our data for DDI2-deficient cells show that fulminant proteotoxic stress also triggers a type I IFN signature (Figure 7). Such signatures are typically observed in interferonopathies such as Aicardy-Goutieres syndrome and proteasomopathies.[47,80,81]

The canonical pathway for IFN activation via cell autonomous innate immune mechanisms relies on the TBK1/IKKε/DDX3 kinases (Figure 7B). Therefore, the TBK1-independent activation of ISGs in DDI2 deficient cells was surprising. However, TBK1 and IKKε redundantly activate IRF3,[82–85] suggesting that IRF3 is likely phosphorylated by IKKε, inducing IFNB and other ISGs (Figure 7E). Furthermore, IRF3 can directly induce the expression of ISGs through ISRE elements in promoter regions.[86–88] The expected STAT1 phosphorylation upon IFN-receptor stimulation was evident only during acute stress induced by BTZ treatment of parental cells. In contrast, we observed only phosphorylated STAT3 in our DDI2-deficient cell models (Figure 7D). This non-canonical signaling likely arises in response to chronic stress, when cells require additional survival mechanisms. In different settings it has been shown that the induction of IFN-signaling in response to proteasome impairment is strongly dependent on PKR.[28,80] Thus, the missing upregulation of PKR in DDI2-deficient embryos may explain the missing IFN-signaling and embryonic death.

JAK-STAT signaling represents a survival pathway involved in stemness, epithelial-mesenchymal transition, and cancerogenesis.[89–93] STAT3, in particular, has been shown to fine-tune type I IFN responses.[94,95] This is important for proper development, because type I IFN signaling impairs stem cell function and potential for differentiation.[96,97] Besides regulating IFN responses, development, and proliferation, STAT3's clinical significance lies in its deleterious oncogenic potential and hyperactivation in various malignancies.[98] Herein, crosstalk occurs between JAK/STAT3 signaling and proliferation pathways such as MAPK/ERK and PI3K/AKT/mTOR,[99] which represent targets for tumor therapy.[100] This cytokine-driven MAPK/ERK signaling may explain the proliferative potential of DDI2 KO cells (Figure 6). In this context, it is important to note that the proteostatic potential of myeloma cells is targeted by proteasome inhibitors that in turn activate the NGLY1-DDI2-TCF11/NRF1 axis, suggesting DDI2 as a promising drug target for multiple myeloma and myeloproliferative neoplasms.[15,18,101–104] Consistent with this idea, EGFR/JAK1/STAT3 signaling contributes to BTZ resistance in multiple myelomas through induction of immunoproteasomes (Figure 4B).[105]

In conclusion, we identified DDI2 as an important regulator of proliferative, developmental, and immune signaling with implications for cancerogenesis. These findings pave the way for further exploration of DDI2's mechanisms and its relationship between proteasome impairment and innate immune signaling. Both the NGLY1-DDI2-TCF11/NRF1 axis and DDI2 itself represent important drug targets. Inhibiting this pathway with new small molecules may contribute to novel chemotherapeutic strategies in cancer treatment, while activators targeting this pathway are urgently needed for conditions linked to proteasome impairment such as neurodegeneration and other proteinopathies.

Limitations of study

The study faced several limitations. One of the primary challenges was early embryonic lethality in the model organisms, which significantly constrained our ability to conduct more extensive analyses. Due to the limited availability of the material, we were unable to perform detailed investigations that could have provided deeper insights into the biological roles of DDI2 during early development. This limitation suggests that future research should consider employing conditional knockout models, which would allow for tissue-specific deletions of DDI2, thereby overcoming the obstacles posed by embryonic lethality and enabling a more focused exploration of its functions in different tissues.

Given DDI2's known role in DNA repair, there is a possibility that other underlying genetic mutations or genomic instability could have influenced the outcomes observed in our cell knockout models. This presents a challenge in definitively attributing the observed phenotypes solely to DDI2 deficiency. Future studies should consider employing complementary approaches, such as whole-genome sequencing, to rule out confounding factors and to better isolate the specific contributions of DDI2 to cellular phenotypes.

While our study primarily focused on the interaction between DDI2 and NRF1, the potential NRF1-independent functions of DDI2 remain largely unexplored. To address this gap, future research could benefit from transcriptional profiling techniques such as RNA-seq. This approach would allow for a comprehensive analysis of gene expression changes in DDI2-deficient cells, potentially uncovering novel pathways and mechanisms regulated by DDI2 that are independent of NRF1. Such data could provide a broader understanding of DDI2's role in cellular homeostasis and stress responses.

RESOURCE AVAILABILITY

Lead contact

Further information and requests for resources and reagents should be directed to and will be fulfilled by the Lead Contact, Klara Grantz Saskova (saskova2@natur.cuni.cz).

Materials availability

Plasmids will be provided upon request from Klara Grantz Saskova.

Cell lines will be provided upon request and MTA signing from Elke Krüger and Klara Grantz Saskova.

The mouse line *Ddi2*^{KO} (*C57BL/6NCrl-Ddi2*$^{tm1b(EUCOMM)Hmgu}$*/Ph*) used in this study was generated at the CCP-IMG CAS (Prague, Czech Republic). It has been deposited in the EMMA repository and is available for order via IMPC using ID EM:12340 (https://www.infrafrontier.eu).

The *Ddi2*^{ex6} mouse line (*C57BL/6NCrl-Ddi2*^{em1}*/Ph*) used in this study was also generated at the CCP-IMG CAS and will be deposited in the EMMA repository upon review process.

Both mouse lines are available upon MTA signing from the laboratory of Jan Konvalinka, IOCB Prague.

Data and code availability

- Phenotyping data of the *Ddi2*^{tm1b} strain (*C57BL/6NCrl-Ddi2*$^{tm1b(EUCOMM)Hmgu}$*/Ph*) strain has been deposited at https://www.mousephenotype.org/data/genes/MGI:1917244.
- Original data together with all raw and uncropped native gels and western blots used in the figures of the paper were deposited on Mendelay Data: https://data.mendeley.com/preview/b7s5vgjp9w?a=64917702-17d3-4916-980a-c37c412e1bdd.
- The mass spectrometry proteomics data have been deposited to the ProteomeXchange Consortium via the PRIDE[106] partner repository and are publicly available as of the date of publication with the dataset identifier PXD034079.[107]
- This paper does not report original code.
- Any additional information required to reanalyze the data reported in this paper is available from the lead contact upon request.

ACKNOWLEDGMENTS

The study was funded by the Czech Science Foundation (project no. GA22-16389S) and Charles University (PRIMUS/21/SCI/018) to K.G.S. This work was also supported by the German Research Foundation SFBTR 186/A13 and RTG 2719 to E.K. and S.M. We would like to thank Christian Hentschker for recording

the mass spectrometric data. The authors used services of the Czech Center for Phenogenomics at the Institute of Molecular Genetics supported by the Czech Academy of Sciences RVO 68378050 and by the project LM2023036 Czech Centre for Phenogenomics provided by Ministry of Education, Youth and Sports of the Czech Republic and CZ.02.1.01/0.0/0.0/18_046/0015861 CCP Infrastructure Upgrade II by MEYS and ESIF.

The authors thank Dr. Edward Curtis for language editing. Special thanks go to Karolína Šrámková, Jana Starková, Jaroslav Kurfürst, Dominika Šubová, and Zuzana Kružíková for their excellent technical assistance. The authors also thank Dr. Václav Veverka and Michal Svoboda for help with evaluation of NMR and DSF experiments and help with DDI2 mutagenesis, and to Dr. Vendula Novosadová (IMG Prague) for help with statistical analysis.

AUTHOR CONTRIBUTIONS

Conceptualization, K.G.S., J.K., R.S., and E.K.; study design, M.N., J.P., P.K., K.G.S., and E.K.; methodology, M.N., S.H.M., S.M., M.P., J.P., S.V., E.H., P.K., F.S., K.C., K.G.S., and E.K.; investigation, M.N., S.H.M., M.P., F.S., M.A., P.K., and K.C.; writing—original draft, M.N. and S.H.M.; writing—K.G.S. and E.K.; review and editing, M.N., M.A., S.H.M., S.M., M.P., J.P., F.S., S.V., E.H., P.K., R.S., K.C., J.K., E.K., and K.G.S.; funding acquisition, R.S., J.K., E.K., and K.G.S.; resources, R.S., J.K., E.K., and K.G.S.; supervision, K.G.S. and E.K.

DECLARATION OF INTERESTS

The authors declare that they have no conflict of interest.

STAR★METHODS

Detailed methods are provided in the online version of this paper and include the following:

- KEY RESOURCES TABLE
- EXPERIMENTAL MODEL AND STUDY PARTICIPANT DETAILS
  - Animal models
  - Cell culture and inhibitors
- METHOD DETAILS
  - Generation and characterization of mouse lines
  - Biophysical characterization of $DDI2^{WT}$ and $Ddi2^{ex6}$ proteins
  - Experimental procedures with mouse tissue
  - Experimental procedures with human cell lines
  - Protein analysis
- QUANTIFICATION AND STATISTICAL ANALYSIS

SUPPLEMENTAL INFORMATION

Supplemental information can be found online at https://doi.org/10.1016/j.isci.2024.110893.

Received: March 14, 2024
Revised: March 25, 2024
Accepted: September 3, 2024
Published: September 5, 2024

REFERENCES

1. Collins, G.A., and Goldberg, A.L. (2017). The Logic of the 26S Proteasome. Cell *169*, 792–806. https://doi.org/10.1016/j.cell.2017.04.023.
2. Zhao, J., Garcia, G.A., and Goldberg, A.L. (2016). Control of proteasomal proteolysis by mTOR. Nature *529*, E1–E2. https://doi.org/10.1038/nature16472.
3. Zhao, J., and Goldberg, A.L. (2016). Coordinate regulation of autophagy and the ubiquitin proteasome system by MTOR. Autophagy *12*, 1967–1970. https://doi.org/10.1080/15548627.2016.1205770.
4. Yu, Y., and Hayward, G.S. (2010). The ubiquitin E3 ligase RAUL negatively regulates type i interferon through ubiquitination of the transcription factors IRF7 and IRF3. Immunity *33*, 863–877. https://doi.org/10.1016/j.immuni.2010.11.027.
5. Xu, H., You, M., Shi, H., and Hou, Y. (2015). Ubiquitin-mediated NFkappaB degradation pathway. Cell. Mol. Immunol. *12*, 653–655. https://doi.org/10.1038/cmi.2014.99.
6. Ling, S.C.W., Lau, E.K.K., Al-Shabeeb, A., Nikolic, A., Catalano, A., Iland, H., Horvath, N., Ho, P.J., Harrison, S., Fleming, S., et al. (2012). Response of myeloma to the proteasome inhibitor bortezomib is correlated with the unfolded protein response regulator XBP-1. Haematolosubjectgica *97*, 64–72. https://doi.org/10.3324/haematol.2011.043331.
7. Hipp, M.S., Park, S.H., and Hartl, F.U. (2014). Proteostasis impairment in protein-misfolding and -aggregation diseases. Trends Cell Biol. *24*, 506–514. https://doi.org/10.1016/j.tcb.2014.05.003.
8. Hetz, C. (2012). The unfolded protein response: controlling cell fate decisions under ER stress and beyond. Nat. Rev. Mol. Cell Biol. *13*, 89–102. https://doi.org/10.1038/nrm3270.
9. Pakos-Zebrucka, K., Koryga, I., Mnich, K., Ljujic, M., Samali, A., and Gorman, A.M. (2016). The integrated stress response. EMBO Rep. *17*, 1374–1395. https://doi.org/10.15252/embr.201642195.
10. Hetz, C., Zhang, K., and Kaufman, R.J. (2020). Mechanisms, regulation and functions of the unfolded protein response. Nat. Rev. Mol. Cell Biol. *21*, 421–438. https://doi.org/10.1038/s41580-020-0250-z.
11. Maurel, M., Chevet, E., Tavernier, J., and Gerlo, S. (2014). Getting RIDD of RNA: IRE1 in cell fate regulation. Trends Biochem. Sci. *39*, 245–254. https://doi.org/10.1016/j.tibs.2014.02.008.
12. So, J.S., Hur, K.Y., Tarrio, M., Ruda, V., Frank-Kamenetsky, M., Fitzgerald, K., Koteliansky, V., Lichtman, A.H., Iwawaki, T., Glimcher, L.H., and Lee, A.H. (2012). Silencing of lipid metabolism genes through IRE1alpha-mediated mRNA decay lowers plasma lipids in mice. Cell Metabol. *16*, 487–499. https://doi.org/10.1016/j.cmet.2012.09.004.
13. Radhakrishnan, S.K., Lee, C.S., Young, P., Beskow, A., Chan, J.Y., and Deshaies, R.J. (2010). Transcription Factor Nrf1 Mediates the Proteasome Recovery Pathway after Proteasome Inhibition in Mammalian Cells. Mol. Cell *38*, 17–28. https://doi.org/10.1016/j.molcel.2010.02.029.
14. Northrop, A., Vangala, J.R., Feygin, A., and Radhakrishnan, S.K. (2020). Disabling the Protease DDI2 Attenuates the Transcriptional Activity of NRF1 and Potentiates Proteasome Inhibitor Cytotoxicity. Int. J. Mol. Sci. *21*, 327. https://doi.org/10.3390/ijms21010327.
15. Fassmannová, D., Sedlák, F., Sedláček, J., Špička, I., and Grantz Šašková, K. (2020). Nelfinavir Inhibits the TCF11/Nrf1-Mediated

Proteasome Recovery Pathway in Multiple Myeloma. Cancers *12*, 1065. https://doi.org/10.3390/cancers12051065.
16. Chavarria, C., Zaffalon, L., Ribeiro, S.T., Op, M., Quadroni, M., Iatrou, M.S., Chapuis, C., and Martinon, F. (2023). ER-trafficking triggers NRF1 ubiquitination to promote its proteolytic activation. iScience *26*, 107777. https://doi.org/10.1016/j.isci.2023.107777.
17. Meiners, S., Heyken, D., Weller, A., Ludwig, A., Stangl, K., Kloetzel, P.M., and Krüger, E. (2003). Inhibition of proteasome activity induces concerted expression of proteasome genes and de novo formation of Mammalian proteasomes. J. Biol. Chem. *278*, 21517–21525. https://doi.org/10.1074/jbc.M301032200.
18. Steffen, J., Seeger, M., Koch, A., and Krüger, E. (2010). Proteasomal degradation is transcriptionally controlled by TCF11 via an ERAD-dependent feedback loop. Mol. Cell *40*, 147–158. https://doi.org/10.1016/j.molcel.2010.09.012.
19. Koizumi, S., Irie, T., Hirayama, S., Sakurai, Y., Yashiroda, H., Naguro, I., Ichijo, H., Hamazaki, J., and Murata, S. (2016). The aspartyl protease DDI2 activates Nrf1 to compensate for proteasome dysfunction. Elife *5*, e18357. https://doi.org/10.7554/eLife.18357.
20. Siva, M., Svoboda, M., Veverka, V., Trempe, J.F., Hofmann, K., Kozisek, M., Hexnerova, R., Sedlak, F., Belza, J., Brynda, J., et al. (2016). Human DNA-Damage-Inducible 2 Protein Is Structurally and Functionally Distinct from Its Yeast Ortholog. Sci. Rep. *6*, 30443. https://doi.org/10.1038/srep30443.
21. Tomlin, F.M., Gerling-Driessen, U.I.M., Liu, Y.C., Flynn, R.A., Vangala, J.R., Lentz, C.S., Clauder-Muenster, S., Jakob, P., Mueller, W.F., Ordoñez-Rueda, D., et al. (2017). Inhibition of NGLY1 Inactivates the Transcription Factor Nrf1 and Potentiates Proteasome Inhibitor Cytotoxicity. ACS Cent. Sci. *3*, 1143–1155. https://doi.org/10.1021/acscentsci.7b00224.
22. Nowak, K., Taubert, R.M., Haberecht, S., Venz, S., and Krüger, E. (2018). Inhibition of calpain-1 stabilizes TCF11/Nrf1 but does not affect its activation in response to proteasome inhibition. Biosci. Rep. *38*, BSR20180393. https://doi.org/10.1042/BSR20180393.
23. Sotzny, F., Schormann, E., Kühlewindt, I., Koch, A., Brehm, A., Goldbach-Mansky, R., Gilling, K.E., and Krüger, E. (2016). TCF11/Nrf1-Mediated Induction of Proteasome Expression Prevents Cytotoxicity by Rotenone. Antioxidants Redox Signal. *25*, 870–885. https://doi.org/10.1089/ars.2015.6539.
24. Studencka-Turski, M., Cetin, G., Junker, H., Ebstein, F., and Kruger, E. (2019). Molecular Insight Into the IRE1alpha-Mediated Type I Interferon Response Induced by Proteasome Impairment in Myeloid Cells of the Brain. Front. Immunol. *10*, 2900. https://doi.org/10.3389/fimmu.2019.02900.
25. Kroll-Hermi, A., Ebstein, F., Stoetzel, C., Geoffroy, V., Schaefer, E., Scheidecker, S., Bar, S., Takamiya, M., Kawakami, K., Zieba, B.A., et al. (2020). Proteasome subunit PSMC3 variants cause neurosensory syndrome combining deafness and cataract due to proteotoxic stress. Embo Mol Med. ARTN *12*, e11861. https://doi.org/10.15252/emmm.201911861.
26. Brehm, A., Liu, Y., Sheikh, A., Marrero, B., Omoyinmi, E., Zhou, Q., Montealegre, G., Biancotto, A., Reinhardt, A., Almeida de Jesus, A., et al. (2015). Additive loss-of-function proteasome subunit mutations in CANDLE/PRAAS patients promote type I IFN production. J. Clin. Invest. *125*, 4196–4211. https://doi.org/10.1172/JCI81260.
27. Poli, M.C., Ebstein, F., Nicholas, S.K., de Guzman, M.M., Forbes, L.R., Chinn, I.K., Mace, E.M., Vogel, T.P., Carisey, A.F., Benavides, F., et al. (2018). Heterozygous Truncating Variants in POMP Escape Nonsense-Mediated Decay and Cause a Unique Immune Dysregulatory Syndrome. Am. J. Hum. Genet. *102*, 1126–1142. https://doi.org/10.1016/j.ajhg.2018.04.010.
28. Davidson, S., Yu, C.H., Steiner, A., Ebstein, F., Baker, P.J., Jarur-Chamy, V., Hrovat Schaale, K., Laohamonthonkul, P., Kong, K., Calleja, D.J., et al. (2022). Protein kinase R is an innate immune sensor of proteotoxic stress via accumulation of cytoplasmic IL-24. Sci. Immunol. *7*, eabi6763.
29. Trempe, J.F., Šašková, K.G., Sivá, M., Ratcliffe, C.D.H., Veverka, V., Hoegl, A., Ménade, M., Feng, X., Shenker, S., Svoboda, M., et al. (2016). Structural studies of the yeast DNA damage-inducible protein Ddi1 reveal domain architecture of this eukaryotic protein family. Sci. Rep. *6*, 33671. https://doi.org/10.1038/srep33671.
30. Svoboda, M., Konvalinka, J., Trempe, J.F., and Grantz Saskova, K. (2019). The yeast proteases Ddi1 and Wss1 are both involved in the DNA replication stress response. DNA Repair *80*, 45–51. https://doi.org/10.1016/j.dnarep.2019.06.008.
31. Serbyn, N., Noireterre, A., Bagdiul, I., Plank, M., Michel, A.H., Loewith, R., Kornmann, B., and Stutz, F. (2020). The Aspartic Protease Ddi1 Contributes to DNA-Protein Crosslink Repair in Yeast. Mol. Cell *77*, 1066–1079.e9. https://doi.org/10.1016/j.molcel.2019.12.007.
32. Yip, M.C.J., Bodnar, N.O., and Rapoport, T.A. (2020). Ddi1 is a ubiquitin-dependent protease. Proc. Natl. Acad. Sci. USA *117*, 7776–7781. https://doi.org/10.1073/pnas.1902298117.
33. Dirac-Svejstrup, A.B., Walker, J., Faull, P., Encheva, V., Akimov, V., Puglia, M., Perkins, D., Kümper, S., Hunjan, S.S., Blagoev, B., et al. (2020). DDI2 Is a Ubiquitin-Directed Endoprotease Responsible for Cleavage of Transcription Factor NRF1. Mol. Cell *79*, 332–341.e7. https://doi.org/10.1016/j.molcel.2020.05.035.
34. Collins, G.A., Sha, Z., Kuo, C.L., Erbil, B., and Goldberg, A.L. (2022). Mammalian Ddi2 is a shuttling factor containing a retroviral protease domain that influences binding of ubiquitylated proteins and proteasomal degradation. J. Biol. Chem. *298*, 101875. https://doi.org/10.1016/j.jbc.2022.101875.
35. Chowdhury, A.M.M.A., Katoh, H., Hatanaka, A., Iwanari, H., Nakamura, N., Hamakubo, T., Natsume, T., Waku, T., and Kobayashi, A. (2017). Multiple regulatory mechanisms of the biological function of NRF3 (NFE2L3) control cancer cell proliferation. Sci. Rep. *7*, 12494. https://doi.org/10.1038/s41598-017-12675-y.
36. Ribeiro, S.T., de Gassart, A., Bettigole, S., Zaffalon, L., Chavarria, C., Op, M., Nugraha, K., and Martinon, F. (2022). The protease DDI2 regulates NRF1 activation in response to cadmium toxicity. iScience *25*, 105227. https://doi.org/10.1016/j.isci.2022.105227.
37. Wang, Y., Zhu, Y., Wang, Y., Chang, Y., Geng, F., Ma, M., Gu, Y., Yu, A., Zhu, R., Yu, P., et al. (2023). Proteolytic activation of angiomotin by DDI2 promotes angiogenesis. EMBO J. *42*, e112900. https://doi.org/10.15252/embj.2022112900.
38. Cavo, M., Pantani, L., Pezzi, A., Petrucci, M.T., Patriarca, F., Di Raimondo, F., Marzocchi, G., Galli, M., Montefusco, V., Zamagni, E., et al. (2015). Bortezomib-thalidomide-dexamethasone (VTD) is superior to bortezomib-cyclophosphamide-dexamethasone (VCD) as induction therapy prior to autologous stem cell transplantation in multiple myeloma. Leukemia *29*, 2429–2431. https://doi.org/10.1038/leu.2015.274.
39. Finley, D. (2009). Recognition and Processing of Ubiquitin-Protein Conjugates by the Proteasome. Annu. Rev. Biochem. *78*, 477–513. https://doi.org/10.1146/annurev.biochem.78.081507.101607.
40. Welk, V., Coux, O., Kleene, V., Abeza, C., Trümbach, D., Eickelberg, O., and Meiners, S. (2016). Inhibition of Proteasome Activity Induces Formation of Alternative Proteasome Complexes. J. Biol. Chem. *291*, 13147–13159. https://doi.org/10.1074/jbc.M116.717652.
41. Kruger, E., and Kloetzel, P.M. (2012). Immunoproteasomes at the interface of innate and adaptive immune responses: two faces of one enzyme. Curr. Opin. Immunol. *24*, 77–83. https://doi.org/10.1016/j.coi.2012.01.005.
42. Whitby, F.G., Masters, E.I., Kramer, L., Knowlton, J.R., Yao, Y., Wang, C.C., and Hill, C.P. (2000). Structural basis for the activation of 20S proteasomes by 11S regulators. Nature *408*, 115–120. https://doi.org/10.1038/35040607.
43. Leung, L., Kwong, M., Hou, S., Lee, C., and Chan, J.Y. (2003). Deficiency of the Nrf1 and Nrf2 transcription factors results in early embryonic lethality and severe oxidative stress. J. Biol. Chem. *278*, 48021–48029. https://doi.org/10.1074/jbc.M308439200.
44. Vomund, S., Schafer, A., Parnham, M.J., Brune, B., and von Knethen, A. (2017). Nrf2, the Master Regulator of Anti-Oxidative Responses. Int. J. Mol. Sci. *18*, 2772.
45. Chevillard, G., and Blank, V. (2011). NFE2L3 (NRF3): the Cinderella of the Cap'n'Collar transcription factors. Cell. Mol. Life Sci. *68*, 3337–3348. https://doi.org/10.1007/s00018-011-0747-x.
46. Ebstein, F., Poli Harlowe, M.C., Studencka-Turski, M., and Krüger, E. (2019). Contribution of the Unfolded Protein Response (UPR) to the Pathogenesis of Proteasome-Associated Autoinflammatory Syndromes (PRAAS). Front. Immunol. *10*, 2756. https://doi.org/10.3389/fimmu.2019.02756.
47. Rice, G.I., Melki, I., Frémond, M.L., Briggs, T.A., Rodero, M.P., Kitabayashi, N., Oojageer, A., Bader-Meunier, B., Belot, A., Bodemer, C., et al. (2017). Assessment of Type I Interferon Signaling in Pediatric Inflammatory Disease. J. Clin. Immunol. *37*, 123–132. https://doi.org/10.1007/s10875-016-0359-1.
48. Llamas, E., Alirzayeva, H., Loureiro, R., and Vilchez, D. (2020). The intrinsic proteostasis network of stem cells. Curr. Opin. Cell Biol. *67*, 46–55. https://doi.org/10.1016/j.ceb.2020.08.005.
49. Garcia-Prat, L., Sousa-Victor, P., and Munoz-Canoves, P. (2017). Proteostatic and Metabolic Control of Stemness. Cell Stem

Cell *20*, 593–608. https://doi.org/10.1016/j.stem.2017.04.011.
50. Hipp, M.S., Kasturi, P., and Hartl, F.U. (2019). The proteostasis network and its decline in ageing. Nat. Rev. Mol. Cell Biol. *20*, 421–435. https://doi.org/10.1038/s41580-019-0101-y.
51. Hu, X., Zou, R., Zhang, Z., Ji, J., Li, J., Huo, X.Y., Liu, D., Ge, M.X., Cui, M.K., Wu, M.Z., et al. (2023). UBE4A catalyzes NRF1 ubiquitination and facilitates DDI2-mediated NRF1 cleavage. Biochim. Biophys. Acta. Gene Regul. Mech. *1866*, 194937. https://doi.org/10.1016/j.bbagrm.2023.194937.
52. Vangala, J.R., Sotzny, F., Krüger, E., Deshaies, R.J., and Radhakrishnan, S.K. (2016). Nrf1 can be processed and activated in a proteasome-independent manner. Curr. Biol. *26*, R834–R835. https://doi.org/10.1016/j.cub.2016.08.008.
53. Fujihira, H., Masahara-Negishi, Y., Tamura, M., Huang, C., Harada, Y., Wakana, S., Takakura, D., Kawasaki, N., Taniguchi, N., Kondoh, G., et al. (2017). Lethality of mice bearing a knockout of the Ngly1-gene is partially rescued by the additional deletion of the Engase gene. PLoS Genet. *13*, e1006696. https://doi.org/10.1371/journal.pgen.1006696.
54. Chan, J.Y., Kwong, M., Lu, R., Chang, J., Wang, B., Yen, T.S., and Kan, Y.W. (1998). Targeted disruption of the ubiquitous CNC-bZIP transcription factor, Nrf-1, results in anemia and embryonic lethality in mice. EMBO J. *17*, 1779–1787. https://doi.org/10.1093/emboj/17.6.1779.
55. Sakao, Y., Kawai, T., Takeuchi, O., Copeland, N.G., Gilbert, D.J., Jenkins, N.A., Takeda, K., and Akira, S. (2000). Mouse proteasomal ATPases Psmc3 and Psmc4: genomic organization and gene targeting. Genomics *67*, 1–7. https://doi.org/10.1006/geno.2000.6231.
56. Kent, W.J., Sugnet, C.W., Furey, T.S., Roskin, K.M., Pringle, T.H., Zahler, A.M., and Haussler, D. (2002). The human genome browser at UCSC. Genome Res. *12*, 996–1006. https://doi.org/10.1101/gr.229102.
57. Gray, P.A., Fu, H., Luo, P., Zhao, Q., Yu, J., Ferrari, A., Tenzen, T., Yuk, D.I., Tsung, E.F., Cai, Z., et al. (2004). Mouse brain organization revealed through direct genome-scale TF expression analysis. Science *306*, 2255–2257. https://doi.org/10.1126/science.1104935.
58. Ramirez, J., Lectez, B., Osinalde, N., Sivá, M., Elu, N., Aloria, K., Procházková, M., Perez, C., Martínez-Hernández, J., Barrio, R., et al. (2018). Quantitative proteomics reveals neuronal ubiquitination of Rngo/Ddi1 and several proteasomal subunits by Ube3a, accounting for the complexity of Angelman syndrome. Hum. Mol. Genet. *27*, 1955–1971. https://doi.org/10.1093/hmg/ddy103.
59. Kottemann, M.C., Conti, B.A., Lach, F.P., and Smogorzewska, A. (2018). Removal of RTF2 from Stalled Replisomes Promotes Maintenance of Genome Integrity. Mol. Cell *69*, 24–35.e5. https://doi.org/10.1016/j.molcel.2017.11.035.
60. Yousaf, A., Wu, Y., Khan, R., Shah, W., Khan, I., Shi, Q., and Jiang, X. (2020). Normal spermatogenesis and fertility in Ddi1 (DNA damage inducible 1) mutant mice. Reprod. Biol. *20*, 520–524. https://doi.org/10.1016/j.repbio.2020.08.006.
61. Farmer, S.C., Sun, C.W., Winnier, G.E., Hogan, B.L., and Townes, T.M. (1997). The bZIP transcription factor LCR-F1 is essential for mesoderm formation in mouse development. Genes Dev. *11*, 786–798. https://doi.org/10.1101/gad.11.6.786.
62. Yokoi, M., and Hanaoka, F. (2017). Two mammalian homologs of yeast Rad23, HR23A and HR23B, as multifunctional proteins. Gene *597*, 1–9. https://doi.org/10.1016/j.gene.2016.10.027.
63. Tanaka, K., and Chiba, T. (1998). The proteasome: a protein-destroying machine. Gene Cell. *3*, 499–510. https://doi.org/10.1046/j.1365-2443.1998.00207.x.
64. Ariyama, Y., Shimizu, H., Satoh, T., Tsuchiya, T., Okada, S., Oyadomari, S., Mori, M., and Mori, M. (2007). Chop-deficient mice showed increased adiposity but no glucose intolerance. Obesity *15*, 1647–1656. https://doi.org/10.1038/oby.2007.197.
65. Masuoka, H.C., and Townes, T.M. (2002). Targeted disruption of the activating transcription factor 4 gene results in severe fetal anemia in mice. Blood *99*, 736–745. https://doi.org/10.1182/blood.V99.3.736.
66. Muller-Newen, G., Stope, M.B., Kraus, T., and Ziegler, P. (2017). Development of platelets during steady state and inflammation. J. Leukoc. Biol. *101*, 1109–1117. https://doi.org/10.1189/jlb.1RU0916-391RR.
67. Hamilton, A.M., and Zito, K. (2013). Breaking It Down: The Ubiquitin Proteasome System in Neuronal Morphogenesis. Neural Plast. *2013*, 196848. https://doi.org/10.1155/2013/196848.
68. Boukhalfa, A., Miceli, C., Ávalos, Y., Morel, E., and Dupont, N. (2019). Interplay between primary cilia, ubiquitin-proteasome system and autophagy. Biochimie *166*, 286–292. https://doi.org/10.1016/j.biochi.2019.06.009.
69. Gerhardt, C., Wiegering, A., Leu, T., and Rüther, U. (2016). Control of Hedgehog Signalling by the Cilia-Regulated Proteasome. J. Dev. Biol. *4*, 27. https://doi.org/10.3390/jdb4030027.
70. Baloghova, N., Lidak, T., and Cermak, L. (2019). Ubiquitin Ligases Involved in the Regulation of Wnt, TGF-beta, and Notch Signaling Pathways and Their Roles in Mouse Development and Homeostasis. Genes *10*, 815. https://doi.org/10.3390/genes10100815.
71. Seifert, U., Bialy, L.P., Ebstein, F., Bech-Otschir, D., Voigt, A., Schröter, F., Prozorovski, T., Lange, N., Steffen, J., Rieger, M., et al. (2010). Immunoproteasomes preserve protein homeostasis upon interferon-induced oxidative stress. Cell *142*, 613–624. https://doi.org/10.1016/j.cell.2010.07.036.
72. Ebstein, F., Voigt, A., Lange, N., Warnatsch, A., Schröter, F., Prozorovski, T., Kuckelkorn, U., Aktas, O., Seifert, U., Kloetzel, P.M., and Krüger, E. (2013). Immunoproteasomes are important for proteostasis in immune responses. Cell *152*, 935–937. https://doi.org/10.1016/j.cell.2013.02.018.
73. Jung, T., Hohn, A., and Grune, T. (2014). The proteasome and the degradation of oxidized proteins: Part III-Redox regulation of the proteasomal system. Redox Biol. *2*, 388–394. https://doi.org/10.1016/j.redox.2013.12.029.
74. Yang, K., Huang, R., Fujihira, H., Suzuki, T., and Yan, N. (2018). N-glycanase NGLY1 regulates mitochondrial homeostasis and inflammation through NRF1. J. Exp. Med. *215*, 2600–2616. https://doi.org/10.1084/jem.20180783.
75. Novoa, I., Zhang, Y.H., Zeng, H.Q., Jungreis, R., Harding, H.P., and Ron, D. (2003). Stress-induced gene expression requires programmed recovery from translational repression (vol 22, pg 1180, 2003). EMBO J. *22*, 2307.
76. Bertolotti, A. (2018). The split protein phosphatase system. Biochem. J. *475*, 3707–3723. https://doi.org/10.1042/Bcj20170726.
77. Schneider, K., Nelson, G.M., Watson, J.L., Morf, J., Dalglish, M., Luh, L.M., Weber, A., and Bertolotti, A. (2020). Protein Stability Buffers the Cost of Translation Attenuation following eIF2alpha Phosphorylation. Cell Rep. *32*, 108154. https://doi.org/10.1016/j.celrep.2020.108154.
78. Dalet, A., Arguello, R.J., Combes, A., Spinelli, L., Jaeger, S., Fallet, M., Manh, T.P.V., Mendes, A., Perego, J., Reverendo, M., et al. (2017). Protein synthesis inhibition and GADD34 control IFN-beta heterogeneous expression in response to dsRNA. EMBO J. *36*, 761–782. https://doi.org/10.15252/embj.201695000.
79. Brehm, A., and Krüger, E. (2015). Dysfunction in protein clearance by the proteasome: impact on autoinflammatory diseases. Semin. Immunopathol. *37*, 323–333. https://doi.org/10.1007/s00281-015-0486-4.
80. Ebstein, F., Küry, S., Most, V., Rosenfelt, C., Scott-Boyer, M.P., van Woerden, G.M., Besnard, T., Papendorf, J.J., Studencka-Turski, M., Wang, T., et al. (2023). PSMC3 proteasome subunit variants are associated with neurodevelopmental delay and type I interferon production. Sci. Transl. Med. *15*, eabo3189. https://doi.org/10.1126/scitranslmed.abo3189.
81. Kim, H., de Jesus, A.A., Brooks, S.R., Liu, Y., Huang, Y., VanTries, R., Montealegre Sanchez, G.A., Rotman, Y., Gadina, M., and Goldbach-Mansky, R. (2018). Development of a Validated Interferon Score Using NanoString Technology. J. Interferon Cytokine Res. *38*, 171–185. https://doi.org/10.1089/jir.2017.0127.
82. Perry, A.K., Chow, E.K., Goodnough, J.B., Yeh, W.C., and Cheng, G. (2004). Differential requirement for TANK-binding kinase-1 in type I interferon responses to toll-like receptor activation and viral infection. J. Exp. Med. *199*, 1651–1658. https://doi.org/10.1084/jem.20040528.
83. Tsuzuki, S., Tachibana, M., Hemmi, M., Yamaguchi, T., Shoji, M., Sakurai, F., Kobiyama, K., Kawabata, K., Ishii, K.J., Akira, S., and Mizuguchi, H. (2016). TANK-binding kinase 1-dependent or -independent signaling elicits the cell-type-specific innate immune responses induced by the adenovirus vector. Int. Immunol. *28*, 105–115. https://doi.org/10.1093/intimm/dxv058.
84. Balka, K.R., Louis, C., Saunders, T.L., Smith, A.M., Calleja, D.J., D'Silva, D.B., Moghaddas, F., Tailler, M., Lawlor, K.E., Zhan, Y., et al. (2020). TBK1 and IKK epsilon Act Redundantly to Mediate STING-Induced NF-kappa B Responses in Myeloid Cells. Cell Rep. *31*, 107492. https://doi.org/10.1016/j.celrep.2020.03.056.
85. Miyahira, A.K., Shahangian, A., Hwang, S., Sun, R., and Cheng, G. (2009). TANK-Binding Kinase-1 Plays an Important Role during In Vitro and In Vivo Type I IFN Responses to DNA Virus Infections.

J. Immunol. *182*, 2248–2257. https://doi.org/10.4049/jimmunol.0802466.

86. DeFilippis, V.R., Robinson, B., Keck, T.M., Hansen, S.G., Nelson, J.A., and Früh, K.J. (2006). Interferon regulatory factor 3 is necessary for induction of antiviral genes during human cytomegalovirus infection. J. Virol. *80*, 1032–1037. https://doi.org/10.1128/Jvi.80.2.1032-1037.2006.
87. Ashley, C.L., Abendroth, A., McSharry, B.P., and Slobedman, B. (2019). Interferon-Independent Upregulation of Interferon-Stimulated Genes during Human Cytomegalovirus Infection is Dependent on IRF3 Expression. Viruses-Basel *11*, 246. https://doi.org/10.3390/v11030246.
88. Csumita, M., Csermely, A., Horvath, A., Nagy, G., Monori, F., Göczi, L., Orbea, H.A., Reith, W., and Széles, L. (2020). Specific enhancer selection by IRF3, IRF5 and IRF9 is determined by ISRE half-sites, 5 ' and 3 ' flanking bases, collaborating transcription factors and the chromatin environment in a combinatorial fashion. Nucleic Acids Res. *48*, 589–604. https://doi.org/10.1093/nar/gkz1112.
89. Deschenes-Simard, X., Parisotto, M., Rowell, M.C., Le Calve, B., Igelmann, S., Moineau-Vallee, K., Saint-Germain, E., Kalegari, P., Bourdeau, V., Kottakis, F., et al. (2019). Circumventing senescence is associated with stem cell properties and metformin sensitivity. Aging Cell *18*, e12889. https://doi.org/10.1111/acel.12889.
90. Ganguly, D., Sims, M., Cai, C., Fan, M., and Pfeffer, L.M. (2018). Chromatin Remodeling Factor BRG1 Regulates Stemness and Chemosensitivity of Glioma Initiating Cells. Stem Cell. *36*, 1804–1815. https://doi.org/10.1002/stem.2909.
91. Lu, T., Bankhead, A., Ljungman, M., and Neamati, N. (2019). Multi-omics profiling reveals key signaling pathways in ovarian cancer controlled by STAT3. Theranostics *9*, 5478–5496. https://doi.org/10.7150/thno.33444.
92. Lin, L., Wang, Y., Sun, B., Liu, L., Ying, W., Wang, W., Zhou, Q., Hou, J., Yao, H., Hu, L., et al. (2020). The clinical, immunological and genetic features of 12 Chinese patients with STAT3 mutations. Allergy Asthma Clin. Immunol. *16*, 1–10. https://doi.org/10.1186/s13223-020-00462-w.
93. Jin, J., Liu, J., Chen, C., Liu, Z., Jiang, C., Chu, H., Pan, W., Wang, X., Zhang, L., Li, B., et al. (2016). The deubiquitinase USP21 maintains the stemness of mouse embryonic stem cells via stabilization of Nanog. Nat. Commun. *7*, 13594. https://doi.org/10.1038/ncomms13594.
94. Charras, A., Arvaniti, P., Le Dantec, C., Arleevskaya, M.I., Zachou, K., Dalekos, G.N., Bordon, A., and Renaudineau, Y. (2020). JAK Inhibitors Suppress Innate Epigenetic Reprogramming: a Promise for Patients with Sjogren's Syndrome. Clin. Rev. Allergy Immunol. *58*, 182–193. https://doi.org/10.1007/s12016-019-08743-y.
95. Tsai, M.H., Pai, L.M., and Lee, C.K. (2019). Fine-Tuning of Type I Interferon Response by STAT3. Front. Immunol. *10*, 1448. https://doi.org/10.3389/fimmu.2019.01448.
96. Eggenberger, J., Blanco-Melo, D., Panis, M., Brennand, K.J., and tenOever, B.R. (2019). Type I interferon response impairs differentiation potential of pluripotent stem cells. Proc. Natl. Acad. Sci. USA *116*, 1384–1393. https://doi.org/10.1073/pnas.1812449116.
97. Yu, Q., Katlinskaya, Y.V., Carbone, C.J., Zhao, B., Katlinski, K.V., Zheng, H., Guha, M., Li, N., Chen, Q., Yang, T., et al. (2015). DNA-damage-induced type I interferon promotes senescence and inhibits stem cell function. Cell Rep. *11*, 785–797. https://doi.org/10.1016/j.celrep.2015.03.069.
98. Todoric, J., and Karin, M. (2019). The Fire within: Cell-Autonomous Mechanisms in Inflammation-Driven Cancer. Cancer Cell *35*, 714–720. https://doi.org/10.1016/j.ccell.2019.04.001.
99. Rawlings, J.S., Rosler, K.M., and Harrison, D.A. (2004). The JAK/STAT signaling pathway. J. Cell Sci. *117*, 1281–1283. https://doi.org/10.1242/jcs.00963.
100. Bai, L., Zhou, H., Xu, R., Zhao, Y., Chinnaswamy, K., McEachern, D., Chen, J., Yang, C.Y., Liu, Z., Wang, M., et al. (2019). A Potent and Selective Small-Molecule Degrader of STAT3 Achieves Complete Tumor Regression In Vivo. Cancer Cell *36*, 498–511.e17. https://doi.org/10.1016/j.ccell.2019.10.002.
101. Gu, Y., Wang, X., Wang, Y., Wang, Y., Li, J., and Yu, F.X. (2020). Nelfinavir inhibits human DDI2 and potentiates cytotoxicity of proteasome inhibitors. Cell. Signal. *75*, 109775. https://doi.org/10.1016/j.cellsig.2020.109775.
102. Op, M., Ribeiro, S.T., Chavarria, C., De Gassart, A., Zaffalon, L., and Martinon, F. (2022). The aspartyl protease DDI2 drives adaptation to proteasome inhibition in multiple myeloma. Cell Death Dis. *13*, 475. https://doi.org/10.1038/s41419-022-04925-3.
103. Chen, T., Ho, M., Briere, J., Moscvin, M., Czarnecki, P.G., Anderson, K.C., Blackwell, T.K., and Bianchi, G. (2022). Multiple myeloma cells depend on the DDI2/NRF1-mediated proteasome stress response for survival. Blood Adv. *6*, 429–440. https://doi.org/10.1182/bloodadvances.2020003820.
104. Lei, L., Cao, Q., An, G., Lv, Y., Tang, J., and Yang, J. (2023). DDI2 promotes tumor metastasis and resists antineoplastic drugs-induced apoptosis in colorectal cancer. Apoptosis *28*, 458–470. https://doi.org/10.1007/s10495-022-01796-z.
105. Zhang, X.D., Baladandayuthapani, V., Lin, H., Mulligan, G., Li, B., Esseltine, D.L.W., Qi, L., Xu, J., Hunziker, W., Barlogie, B., et al. (2016). Tight Junction Protein 1 Modulates Proteasome Capacity and Proteasome Inhibitor Sensitivity in Multiple Myeloma via EGFR/JAK1/STAT3 Signaling. Cancer Cell *29*, 639–652. https://doi.org/10.1016/j.ccell.2016.03.026.
106. Perez-Riverol, Y., Bai, J., Bandla, C., García-Seisdedos, D., Hewapathirana, S., Kamatchinathan, S., Kundu, D.J., Prakash, A., Frericks-Zipper, A., Eisenacher, M., et al. (2022). The PRIDE database resources in 2022: a hub for mass spectrometry-based proteomics evidences. Nucleic Acids Res. *50*, D543–D552. https://doi.org/10.1093/nar/gkab1038.
107. Deutsch, E.W., Bandeira, N., Sharma, V., Perez-Riverol, Y., Carver, J.J., Kundu, D.J., García-Seisdedos, D., Jarnuczak, A.F., Hewapathirana, S., Pullman, B.S., et al. (2020). The ProteomeXchange consortium in 2020: enabling 'big data' approaches in proteomics. Nucleic Acids Res. *48*, D1145–D1152. https://doi.org/10.1093/nar/gkz984.
108. Tykvart, J., Bařinka, C., Svoboda, M., Navrátil, V., Souček, R., Hubálek, M., Hradilek, M., Šácha, P., Lubkowski, J., and Konvalinka, J. (2015). Structural and Biochemical Characterization of a Novel Aminopeptidase from Human Intestine. J. Biol. Chem. *290*, 11321–11336. https://doi.org/10.1074/jbc.M114.628149.
109. Cermak, T., Doyle, E.L., Christian, M., Wang, L., Zhang, Y., Schmidt, C., Baller, J.A., Somia, N.V., Bogdanove, A.J., and Voytas, D.F. (2011). Efficient design and assembly of custom TALEN and other TAL effector-based constructs for DNA targeting. Nucleic Acids Res. *39*, e82. https://doi.org/10.1093/nar/gkr218.
110. Doyle, E.L., Booher, N.J., Standage, D.S., Voytas, D.F., Brendel, V.P., VanDyk, J.K., and Bogdanove, A.J. (2012). TAL Effector-Nucleotide Targeter (TALE-NT) 2.0: tools for TAL effector design and target prediction. Nucleic Acids Res. *40*, W117–W122. https://doi.org/10.1093/nar/gks608.
111. Flemr, M., Malik, R., Franke, V., Nejepinska, J., Sedlacek, R., Vlahovicek, K., and Svoboda, P. (2013). A retrotransposon-driven dicer isoform directs endogenous small interfering RNA production in mouse oocytes. Cell *155*, 807–816. https://doi.org/10.1016/j.cell.2013.10.001.
112. Kasparek, P., Krausova, M., Haneckova, R., Kriz, V., Zbodakova, O., Korinek, V., and Sedlacek, R. (2014). Efficient gene targeting of the Rosa26 locus in mouse zygotes using TALE nucleases. FEBS Lett. *588*, 3982–3988. https://doi.org/10.1016/j.febslet.2014.09.014.
113. Wilkinson, D.G., and Nieto, M.A. (1993). Detection of Messenger-Rna by in-Situ Hybridization to Tissue-Sections and Whole Mounts. Method Enzymol *225*, 361–373.
114. Blankenburg, S., Hentschker, C., Nagel, A., Hildebrandt, P., Michalik, S., Dittmar, D., Surmann, K., and Völker, U. (2019). Improving Proteome Coverage for Small Sample Amounts: An Advanced Method for Proteomics Approaches with Low Bacterial Cell Numbers. Proteomics *19*, e1900192. https://doi.org/10.1002/pmic.201900192.
115. Gillespie, M., Jassal, B., Stephan, R., Milacic, M., Rothfels, K., Senff-Ribeiro, A., Griss, J., Sevilla, C., Matthews, L., Gong, C., et al. (2022). The reactome pathway knowledgebase 2022. Nucleic Acids Res. *50*, D687–D692. https://doi.org/10.1093/nar/gkab1028.
116. Griss, J., Viteri, G., Sidiropoulos, K., Nguyen, V., Fabregat, A., and Hermjakob, H. (2020). ReactomeGSA-Efficient Multi-Omics Comparative Pathway Analysis. Mol. Cell. Proteomics *19*, 2115–2125. https://doi.org/10.1074/mcp.TIR120.002155.
117. Jassal, B., Matthews, L., Viteri, G., Gong, C., Lorente, P., Fabregat, A., Sidiropoulos, K., Cook, J., Gillespie, M., Haw, R., et al. (2020). The reactome pathway knowledgebase. Nucleic Acids Res. *48*, D498–D503. https://doi.org/10.1093/nar/gkz1031.

STAR★METHODS

KEY RESOURCES TABLE

REAGENT or RESOURCE	SOURCE	IDENTIFIER
Antibodies		
Rabbit monoclonal anti-TCF11/NRF1 (clone D5B10)	Cell Signaling Technology	Cat# 8052S; RRID: AB_11178947
Rabbit polyclonal anti-DDI2	Abcam	Cat# ab197081; RRID: AB_11179454
Rabbit polyclonal anti-NRF2 (clone H300)	Santa Cruz Biotechnology	Cat# sc-13032; RRID: AB_2260102
Mouse monoclonal anti-HO-1 (clone HO-1-1)	Enzo Life Sciences	Cat# ADI-OSA-110-D; RRID: AB_2039355
Mouse monoclonal anti-α-Tubulin (clone DM1A)	Abcam	Cat# ab7291; RRID: AB_449225
Rabbit monoclonal anti-CREB (clone 48H2)	Cell Signaling Technology	Cat# 9197S; RRID: AB_2071899
Rabbit monoclonal anti-Histone H3 (clone D1H2)	Cell Signaling Technology	Cat# 4499S; RRID: AB_10549700
Mouse monoclonal anti-Calnexin (clone AF18)	Invitrogen	Cat# MA3-027; RRID: AB_325404
Rabbit monoclonal anti-ATF4 (clone D4B8)	Cell Signaling Technology	Cat# 11815S; RRID: AB_2281817
Mouse monoclonal anti-CHOP (clone L63F7)	Cell Signaling Technology	Cat# 2895S; RRID: AB_2071893
Rabbit polyclonal anti-eIF2α	Cell Signaling Technology	Cat# 9722S; RRID: AB_2096481
Rabbit polyclonal anti-Phospho-eIF2α (Ser51)	Cell Signaling Technology	Cat# 9721S; RRID: AB_2096482
Rabbit monoclonal anti-ATF6 (clone D4Z8V)	Cell Signaling Technology	Cat# 65880S; RRID: AB_2566413
Rabbit monoclonal anti-PERK (clone C33E10)	Cell Signaling Technology	Cat# 3192S; RRID: AB_2092513
Rabbit monoclonal anti-Phospho-PERK (Thr980; clone 16F8)	Cell Signaling Technology	Cat# 3179S; RRID: AB_2095679
Mouse monoclonal anti-PKR (clone B-10)	Santa Cruz Biotechnology	Cat# sc-6282; RRID: AB_632050
Rabbit monoclonal anti-PKR (clone D7F7)	Cell Signaling Technology	Cat# 12297; RRID: AB_10989188
Rabbit polyclonal anti-Phospho-PKR (Thr446)	Abcam	Cat# ab226852; RRID: AB_2687004
Rabbit polyclonal anti-Phospho-PKR (Thr451)	Invitrogen	Cat# 44-668G; RRID: AB_10980464
Rabbit polyclonal anti-STAT1	Cell Signaling Technology	Cat# 9172S; RRID: AB_330922
Rabbit monoclonal anti-Phospho-STAT1 (Tyr701; clone S.213.5)	Invitrogen	Cat# MA5-15071; RRID: AB_10985495
Mouse monoclonal anti-STAT3	Abcam	Cat# ab50761; RRID: AB_869285
Rabbit polyclonal anti-Phospho-STAT3	Cell Signaling Technology	Cat# 9131S; RRID: AB_10694257
Rabbit polyclonal anti-TBK1	Cell Signaling Technology	Cat# 3013; RRID: AB_2199749
Rabbit monoclonal anti-Phospho-TBK1 (Ser172; clone D52C2)	Cell Signaling	Cat# 5483S; RRID: AB_10693494
Rabbit polyclonal anti-Phospho-IKKε (Ser172)	Merck	Cat# 06-1340; RRID: AB_1977000
Rabbit monoclonal anti-IKKε (clone JU06-72)	Invitrogen	Cat# MA5-32807; RRID: AB_2848260
Rabbit monoclonal anti-IRF3 (D83B9)	Cell Signaling Technology	Cat# 4302S; RRID: AB_10693982
Rabbit monoclonal anti-Phospho-IRF3 (Ser396; clone 4D4G)	Cell Signaling Technology	Cat# 4947S; RRID: AB_10694290
Rabbit monoclonal anti-K48-linkage Specific Polyubiquitin (clone D9D5)	Cell Signaling Technology	Cat# 8081S; RRID: AB_11179017
Rabbit polyclonal anti- α4 (378)	Laboratory stock	N/A
Mouse monoclonal anti-α6 (clone MCP20)	Enzo Life Sciences	Cat# BML-PW8100; RRID: AB_2051189
Mouse monoclonal anti-LMP7 (clone A12)	Santa Cruz Biotechnology	Cat# sc-365699; RRID: AB_2168508
Mouse monoclonal anti-RPT6 (clone p45-110)	Enzo Life Sciences	Cat# BML-PW9265; RRID: AB_2050351
Mouse monoclonal anti-RPN5 (clone H3)	Santa Cruz Biotechnology	Cat# sc-398279; RRID: AB_2157594
Rabbit polyclonal anti-PA28α (K232/1)	Laboratory stock	N/A
Rabbit polyclonal anti-PA28β	Cell Signaling Technology	Cat# 2409S; RRID: AB_10694424
Anti-rabbit IgG, HRP-linked Antibody	Cell Signaling Technology	Cat# 7074S; RRID: AB_2099233
Anti-mouse IgG, HRP-linked Antibody	Cell Signaling Technology	Cat# 7076S; RRID: AB_330924
Anti-Digoxigenin-AP, Fab fragments	Merck Roche	Cat# 11093274910; RRID: AB_2311813

(*Continued on next page*)

Continued

REAGENT or RESOURCE	SOURCE	IDENTIFIER
Rabbit anti-DDI2 Antibody	Bethyl	Cat# A304-630A; RRID: AB_2783793
Anti-β-Actin antibody, Mouse monoclonal, clone AC-15	Sigma Aldrich	Cat# A1978; RRID: AB_476692
IRDye® 680RD Goat anti-Mouse IgG Secondary Antibody	LI-COR Biotechnology	Cat# 926-68070; RRID: AB_10956588
IRDye® 800CW Goat anti-Rabbit IgG Secondary Antibody	LI-COR Biotechnology	Cat# 926-32211; RRID: AB_10693535
Bacterial and virus strains		
E. coli BL21(DE3)RIL	Agilent Technologies	Cat# 230245
Chemicals, peptides, and recombinant proteins		
Bortezomib HEXAL® (3.5 mg, clinical grade)	Hexal	ATC L01XX32
Suc-LLVY-AMC	Bachem	Cat# 4011369
Endonuclease *S. marcescens*	Protean	Cat# 1193
ROTI®Block 10×	Carl Roth	Cat# A151.1
Restore™ Western Blot Stripping-Puffer	Thermo Fisher Scientific	Cat# 21063
Clarity Western ECL Substrate	Bio-Rad	Cat# 1705061
peqGOLD TriFast™	VWR Peqlab	Cat# 30-2010
DirectPCR Lysis Reagent	Viagen	Cat# 102-T
Proteinase K	New England Biolabs	Cat# P8107S
X-Gal	Thermo Fisher Scientific	Cat# R0404
Nuclear Fast Red	Sigma-Aldrich	Cat# 60700
Aquatex	Merck Millipore	Cat# 1085620050
BM-Purple	Merck Roche	Cat# 11442074001
RNA later®	Sigma-Aldrich	Cat# R0901
MG132	Calbiochem	Cat# 474790
cOmpleteTM Mini protease inhibitor cocktail, EDTA free	Merck Roche	Cat# 11836170001
Benzonase® Nuclease	Sigma-Aldrich	Cat# E1014-5KU
Benzonase® Nuclease (Novagen®)	Merck Millipore	Cat# 70664
M-MLV Reverse Transcriptase	Promega	Cat# M170B
SYPRO® Orange protein gel stain	Sigma-Aldrich	Cat# S5692
TEV protease	This study	N/A
jetPRIME® Transfection Reagent	Polyplus	Cat# 114-15
Trypsin	Promega	V5111
Critical commercial assays		
Premix Ex Taq™ (Probe qPCR)	Takara	Cat# RR390L
Human *RPLP0* TaqMan™ Probe	Applied Biosystems	Cat# 4331182; Hs99999902_m1
Human *PSMA2* TaqMan™ Probe	Applied Biosystems	Cat# 4331182; Hs00855061_sH
Human *PSMB6* TaqMan™ Probe	Applied Biosystems	Cat# 4331182; Hs00382586_m1
Human *PSMC4* TaqMan™ Probe	Applied Biosystems	Cat# 4331182; Hs00197826_m1
Human *PSME2* TaqMan™ Probe	Applied Biosystems	Cat# 4331182; Hs01923165_u1
Human *NFE2L1* TaqMan™ Probe	Applied Biosystems	Cat# 4331182; Hs00231457_m1
Human *NFE2L2* TaqMan™ Probe	Applied Biosystems	Cat# 4331182; Hs00975960_m1
Human *ATF4* TaqMan™ Probe	Applied Biosystems	Cat# 4331182; Hs00909569_g1
Human *DDIT3* TaqMan™ Probe	Applied Biosystems	Cat# 4331182; Hs00358796_g1
Human *GRP94* TaqMan™ Probe	Applied Biosystems	Cat# 4331182; Hs00427665_g1
Human *ISG15* TaqMan™ Probe	Applied Biosystems	Cat# 4331182; Hs00192713_m1
Human *USP18* TaqMan™ Probe	Applied Biosystems	Cat# 4331182; Hs00276441_m1
Human *OASL* TaqMan™ Probe	Applied Biosystems	Cat# 4331182; Hs00388714_m1

(*Continued on next page*)

Continued

REAGENT or RESOURCE	SOURCE	IDENTIFIER
Human *IFI44* TaqMan™ Probe	Applied Biosystems	Cat# 4331182; Hs00951349_m1
Human *IFI44L* TaqMan™ Probe	Applied Biosystems	Cat# 4331182; Hs00915292_m1
Human *IFI27* TaqMan™ Probe	Applied Biosystems	Cat# 4331182; Hs01086373_g1
Human *IFIT1* TaqMan™ Probe	Applied Biosystems	Cat# 4331182; Hs00356631_g1
Human *IFNB1* TaqMan™ Probe	Applied Biosystems	Cat# 4331182; Hs01077958_s1
Mouse Direct PCR Kit	Bimake	Cat# B40015
Agilent RNA 6000 Nano Kit	Agilent Technologies	Cat# 5067-1511
TATAA GrandScript cDNA Synthesis Kit	TATAA Biocenter	Cat# A103b
TATAA SYBR® GrandMaster® Mix	TATAA Biocenter	Cat# TA01-625
Experimental models: Cell lines		
Human endothelial: EAhy926 cells	ATCC	RRID:CVCL_3901
Human endothelial: EAhy926 *DDI2* knock-out cells	Nowak et al., 2018[22]	N/A
Human: HEK293-TetOff-A2 cells	Tykvart et al., 2015[108]	N/A
Experimental models: Organisms/strains		
C57BL/6Ncrl	CRL	RRID:IMSR_CRL:027
C57BL/6NCrl-Ddi2$^{tm1b(EUCOMM)Hmgu}$/Ph	This study	Cat# EM:12340, RRID:IMSR_EM:12340
C57BL/6NCrl-Ddi2^{em1}/Ph	This study	N/A
Oligonucleotides		
Random primers	Promega	Cat# C118A
Primers for off-target screen, see Table S2	This study	N/A
Primers for genotyping, see Table S3	This study	N/A
Primers for ISH, see Table S4	This study	N/A
Probe used in RT-PCR screening, see Table S5	This study	N/A
Recombinant DNA		
p905_mDDI2_WT	This study	N/A
p905_mDDI2_Δ256-294	This study	N/A
pTreTight	Clontech	N/A
pTreTight_mDDI2_WT	This study	N/A
pTreTight_mDDI2_Δ256-294	This study	N/A
pTreTight _DDI2_D252A	Sivá et al.[20]	N/A
pTreTight _DDI2_D252N	This study	N/A
pcDNA3.1	Invitrogen	Cat# V79020
pcDNA3.1/V5-His-TOPO_DDI2_WT	This study	N/A
pcDNA3.1/V5-His-TOPO_DDI2_D252A	This study	N/A
pcDNA3.1/V5-His-TOPO_DDI2_D252N	This study	N/A
Software and Algorithms		
Photoshop CS6	Adobe	https://www.adobe.com/de/products/photoshop.html Adobe Photoshop (RRID:SCR_014199)
GraphPad Prism 10	GraphPad Software	https://www.graphpad.com/ GraphPad Prism (RRID:SCR_002798)
ImageJ 1.47v	NIH	https://imagej.nih.gov/ij/ImageJ (RRID:SCR_003070)
GenEx™	MultiD Analyses AB	https://multid.se/genex/

(*Continued on next page*)

Continued

REAGENT or RESOURCE	SOURCE	IDENTIFIER
Topspin 3.2	Bruker	https://www.bruker.com/products/mr/nmr/software/topspin.html TopSpin (RRID:SCR_014227)
LightCycler® 480 SW 1.5.1	Roche	https://lifescience.roche.com/en_de/products/lightcycler14301-480-software-version-15.html LightCycler Software (RRID:SCR_012155)
Xcalibur software	Thermo Fisher Scientific	https://www.thermofisher.com/order/catalog/product/de/de/OPTON-30965 Thermo Xcalibur (RRID:SCR_014593)
Proteome Discoverer 2.4	Thermo Fisher Scientific	https://www.thermofisher.com/de/de/home/industrial/mass-spectrometry/liquid-chromatography-mass-spectrometry-lc-ms/lc-ms-software/multi-omics-data-analysis/proteome-discoverer-software.html Proteome Discoverer (RRID:SCR_014477)
ProteomeXchange Consortium via the PRIDE partner repository with the dataset identifier		ProteomeXchange (RRID:SCR_004055) Identifier: PXD034079
R version 4.0.2	R Core Team	http://www.R-project.org/R Project for Statistical Computing (RRID:SCR_001905)
TAL Effector Nucleotide Targeter 2.0	Cermak T. et al., 2011[109]; Doyle E. L. et al., 2012[110]	https://tale-nt.cac.cornell.edu/node/add/single-tale https://doi.org/10.1093/nar/gks608
BioRender	BioRender	https://app.biorender.com Biorender (RRID:SCR_018361)
Other		
NativePAGE™ Bis-Tris gel 3–12%, non-denaturing	Invitrogen	Cat# BN1001BOX
Immobilon-P PVDF membrane 0.45 μm	Merck Millipore	Cat# IPVH00010
Nitrocellulose Membrane	Bio-Rad	Cat# 1620115
RP NEW/UV film	CEA	Cat# EC84A
IMDM	PAN-Biotech	Cat# P04-20450
IMDM	Thermo Fischer Scientific	Cat# 12440053
opti-MEM medium	Thermo Fischer Scientific	Cat# 31985062
L-glutamine	Sigma Aldrich	Cat# G3126
10% v/v fetal bovine serum	PAN-Biotech	Cat# P30-3306
Penicilin/streptomycin 10 000 U/10 mg/mL	PAN-Biotech	Cat# P06-07100
mMESSAGE mMACHINE T7 kit	Thermo Fischer Scientific	Cat# AM1344
Poly(A) Tailing Kit	Thermo Fisher Scientific	Cat# AM1350
RNeasy plus Micro kit	QIAGEN	Cat# 74034
RNeasy Mini kit	QIAGEN	Cat# 74106
Polyethylenimine	Sigma Aldrich	Cat# 408727
Ni-NTA Agarose	QIAGEN	Cat# 30210
DynaMag™-2 Magnet	Thermo Fischer	12321D
Sera-Mag™ SpeedBead Carboxylate-Modified [E7] Magnetic Particles	Cytiva	45152105050250
Sera-Mag™ SpeedBead Carboxylate-Modified [E3] Magnetic Particles	Cytiva	65152105050250
TALEN sequences, see Table S1	This study	N/A

EXPERIMENTAL MODEL AND STUDY PARTICIPANT DETAILS

Animal models

C57BL/6NCrl mouse strain animals used for either colony management or experiments were purchased from animal facility of the Institute of Molecular Genetics of the Czech Academy of Science (IMG CAS, Prague, Czech Republic).

The *Ddi2*^{KO} strain (*C57BL/6NCrl-Ddi2*$^{tm1b(EUCOMM)Hmgu}$*/Ph*, RRID: IMSR_EM:12340) originates from the ES cell clone HEPD0660_5_E02 of The European Conditional Mouse Mutagenesis Program (EUCOMM). It was generated for this study by the CCP-IMG CAS (Prague, Czech Republic) by crossing *Gt(ROSA)26Sor*$^{tm1(ACTB-cre,-EGFP)Ics}$) and *Ddi2*^{tm1a} (*C57BL/6NCrl-Ddi2*$^{tm1a(EUCOMM)Hmgu}$*/Ph*) mice. The double-heterozygous offspring obtained in this cross were then crossed to *C57BL/6NCrl* wild-type mice and further maintained in this background.

The *Ddi2*^{ex6} strain (*C57BL/6NCrl-Ddi2*^{em1}*/Ph*) was generated in this study by TALEN-mediated genome editing and maintained in *C57BL/6Ncrl* background.

All mice were housed in IVC cages in the SPF animal facility at the Institute of Molecular Genetics of the Czech Academy of Science (Prague, Czech Republic). The animal subjects involved in this study were mouse embryos at midgestation developmental period between E9.5-E15.5. The sex of the embryos was not determined, as it was not relevant to the objectives of the study, which focused on basal cellular mechanisms that are not influenced by sex or gender. All experiments were approved by the Animal Care Committee of the IMG CAS according to institutional and national guidelines of the Czech Central Commission for Animal Welfare and in accordance with European directive 2010/63/EU.

Cell culture and inhibitors

EAhy926 cells (RRID:CVCL_3901) were purchased from ATCC (CRL-2922). Generation of *DDI2* KO EAhy926 cells was previously described.[22] Cells were cultured in Iscove's Modified Dulbecco's Medium (IMDM; PAN-Biotech) supplemented with 10% v/v fetal bovine serum (FBS; PAN-Biotech), 100 U/ml penicillin and 100 μg/mL streptomycin (PAN-Biotech). Cells were grown at 37°C, 5% CO_2 and 95% humidity and routinely passaged 2 times a week.

Proteasomal activity was inhibited using 50 nM water-soluble bortezomib (BTZ; Velcade, Hexal) for the indicated period of time.

HEK293-TetOff-A2 cells were created in the laboratory of Jan Konvalinka.[108] Cells were cultured in IMDM complete medium (Thermo Fisher Scientific), 10% FBS and 40 mM L-glutamine (Sigma-Aldrich) at 37°C, 5% CO2 and 95% humidity and routinely passaged 2 times a week.

METHOD DETAILS

Generation and characterization of mouse lines

Generation of the C57BL/6NCrl-Ddi2^{ex6} *mouse line*

Exon 6 of the *Ddi2* gene was excised using TAL Effector Nucleotide Targeter 2.0[109] Briefly, TALENs were assembled using the Golden Gate Cloning system[109]), cloned into the ELD-KKR backbone plasmid[111] and transcribed into mRNAs using the mMESSAGE mMACHINE T7 kit (Thermo Fisher Scientific). TALEN mRNAs were polyadenylated with the Poly(A) Tailing kit (Thermo Fisher Scientific), purified using the RNeasy mini kit (QIAGEN) and microinjected into male nucleoli of zygotes isolated from *C57BL/6N* mice as previously described.[112] For the off-target control, the F1 generation mice used for colony establishment were screened for twelve possible TALEN off-target sites on chromosome 4 predicted by the TAL Effector Nucleotide Targeter 2.0[112] by PCR amplification and sequencing. Sequences of TALENs are provided in Table S1. Sequences of primers used in the off-target screen are provided in Table S2.

Genotyping of animals

Mice and embryos were genotyped from a gDNA template isolated from the tail-tip, ear or yolk sac by overnight incubation at 55°C with DirectPCR Lysis Reagent (Viagen) and Proteinase K (New England Biolabs). PCR reactions were performed using the Mouse Direct PCR Kit (Bimake). Primers Ddi2F and Ddi2R were used for genotyping of *Ddi2*^{ex6} strain samples. In cases of inefficient amplification during the first round of PCR, mainly when DNA was purified from small bits of yolk sac tissue, two rounds of nested PCR were added to the genotyping procedure. In Nested PCR 1, primers in closer proximity to exon 6 were used (Ddi2 nested F, Ddi2 long R). Nested PCR 2 was designed with a reverse primer (Ddi2 IN R) inside exon 6. Primers LacZ F, Ddi2^{tm1b} WT F and Ddi2^{tm1b} RV were used for genotyping of the *Ddi2*^{tm1b} strain. Primer sequences are listed in Table S3 in the supplemental information.

Phenotyping of adult mice

Phenotyping of adult heterozygous mice of both strains was performed in collaboration with the CCP- IMG CAS according to the International Mouse Phenotyping Consortium (IMPC) pipeline workflow and standard operating procedures (available at https://www.mousephenotype.org/).

A *Ddi2*^{tm1b} mouse cohort (7 *Ddi2*$^{+/-}$ males and 8 *Ddi2*$^{+/-}$ females) was analyzed with respect to body composition and weight, performance in behavioral, cardiovascular and lung function tests, hematology and biochemistry, glucose metabolism (IpGTT), gross pathology, and histology after termination. The results were compared to those of a *C57BL/6NCrl* reference cohort housed at the IMG CAS.

Ddi2$^{ex6+/-}$ mice (8 of each sex) were studied for glucose metabolism (IpGTT), hematology, biochemistry, gross pathology and histology after termination. The results for *Ddi2*$^{ex6+/-}$ mice were compared to values from a cohort of *Ddi2*$^{ex6+/+}$ mice of the same size and a *C57BL/6NCrl* cohort housed at IMG CAS.

MicroCT

Embryos of the *Ddi2*-deficient strains and the control strain *C57BL/6NCrl* were harvested at stages E10.5 and E11.5, fixed in 4% PFA for 3 days and immersed in the contrasting agent 1% phosphotungstic acid for 1 week. Contrasted specimens were embedded in 2.5% low gelling temperature agarose dissolved in water. Scans were performed using a SkyScan 1272 high-resolution microCT (Bruker) with the resolution set to 1.2 μm.

Biophysical characterization of DDI2^{WT} and Ddi2^{ex6} proteins

Cloning, recombinant protein expression and purification

Murine DDI2^{WT} (residues 1–399) and DDI2^{ex6} (Δ256-294) protein coding sequences were amplified by PCR from cDNA acquired from embryonal tissue. RNA isolation and reverse transcription were performed as described in the STAR Methods section "*Ddi2* expression analysis in mouse embryos using qRT-PCR." Constructs encoding the DDI2^{WT} and DDI2^{ex6} proteins were cloned into p905 (gift from Pavlína Řezáčová, IOCB CAS, Prague) and pTreTight (Clontech) expression vectors.

p905 bacterial expression vectors encoding DDI2^{WT} and DDI2^{ex6} were expressed in BL21(DE3)RIL host cells (Novagen). These proteins, which are in frame with an N-terminal histidine tag, were purified by two rounds of nickel affinity chromatography using Ni-NTA agarose (QIAGEN), with overnight cleavage by N-terminally His-tagged TEV protease (expressed in our laboratory) in-between. The later flow-through fraction containing the desired protein was further purified by size-exclusion chromatography in 50 mM sodium phosphate buffer pH 7.4, 0.5% (v/v) glycerol by FPLC (ÄKTA explorer, Amersham Pharmacia Biotech) using a Superdex 200pg 16/60 FPLC column (GE Healthcare). Final protein fractions were analyzed by SDS-PAGE electrophoresis.

1D NMR

The ^{1}H HSQC spectra of DDI2^{WT} and DDI2^{ex6} were acquired using 350 μL of 50 μM protein samples in 50 mM phosphate buffer at pH 7.4 with 0.5% glycerol at 25°C on a 600 MHz Bruker Avance spectrometer (Bruker BioSpin GmbH) equipped with a triple resonance (^{15}N, ^{13}C, ^{1}H) cryoprobe. Spectra were processed using Topspin 3.2 (Bruker).

Differential scanning fluorimetry (DSF)

DSF experiments were performed using 20 μM final concentration of DDI2^{ex6} and DDI2^{WT} proteins in 50 mM phosphate buffer pH 7.4, 0.5% glycerol with 5000× diluted SYPRO Orange protein gel stain (Sigma-Aldrich) in total reaction volume 25 μL. The thermofluor assay and calculation of melting temperatures were performed on a LightCycler 480 II using LightCycler 480 Software (Roche).

Experimental procedures with mouse tissue

β-galactosidase activity detection

For mapping of *Ddi2* expression using the β-galactosidase activity detection method, *Ddi2*$^{+/-}$ adult mice of both sexes (age: 16 weeks) and embryos at the embryonal stages E9.5, E10.5, E12.5, and E14.5 were harvested. Embryos and adult tissue used for whole mount staining were fixed in 4% PFA and thoroughly washed in 1 M phosphate buffer pH 7.5, 0.5 M EGTA, 0.01% sodium deoxycholate, 2 mM $MgCl_2$, and 0.02% Nonidet P-40. They were then stained overnight at 37°C in the dark in X-gal staining solution containing 0.1 M phosphate buffer pH 7.5, 0.02% Nonidet P-40, 0.01% sodium deoxycholate, 5 mM potassium ferricyanide, 5 mM potassium ferrocyanide, 2 mM $MgCl_2$, and 1 mg/ml X-Gal (Thermo Fisher Scientific), rinsed in PBS and post-fixed in 4% PFA prior to imaging.

Embryos used for sectioning were embedded in 30% sucrose/PBS overnight and frozen in OCT prior to cryo-sectioning (10 μm sagittal sections) according to standard operating protocols of the Czech Center for Phenogenomics. Following washing and staining, procedures were performed as for whole mount staining. After post-fixation in 4% PFA, slides were washed in PBS, counter-stained with Nuclear Fast Red (Sigma-Aldrich) and mounted in Aquatex (Merck Millipore). Imaging of sections was performed using a Zeiss AxioImager Z2 and a Zeiss AxioScan Z1. Zeiss AxioZoom with Apotome module macroscope was used for whole mount imaging.

RNA in situ hybridization

Specific types of tissues from adult mice and whole embryos of the *C57BL/6NCrl* strain at the E9.5, E10.5 and E11.5 stages were harvested and processed as either paraffin sections or as whole-mount samples. Adult tissues were fixed in 4% PFA, embedded in paraffin, and sectioned at 7μm. Whole-mount embryos were fixed in 4% PFA and frozen in methanol at −20°C, which was followed by tissue hydration, proteinase K treatment, acetylation, and pre-hybridization as previously described.[113] Solutions were prepared with RNAse free water. Hybridization on sections was performed overnight at 70°C with DIG-labeled probes in hybridization buffer (1.25X saline sodium citrate, pH 7.0, 50% formamide, 0.1% Tween 20, 100X Denhardt's solution, heparin (50 μg/mL), tRNA (50 μg/mL), and salmon sperm DNA (50 μg/mL)). Hybridization on whole-mount embryos was performed overnight at 69°C with DIG-labeled probes in hybridization buffer (5X saline sodium citrate, pH 7.0, 50% formamide, 0.1% Tween 20, 1X Denhardt's solution, heparin (50 μg/mL), and tRNA (50 μg/mL), and salmon sperm DNA (50 μg/mL)). Digoxygenin-labeled RNA probes (DIG RNA labeling kit, Roche) were generated by *in vitro* transcription from a PCR-amplified fragment of murine *Ddi2*. The sequence of the *Ddi2* antisense probe is shown in Table S4 in the Appendix. The sense probe with complementary sequence was used as a negative control. An anti-DIG antibody conjugated to alkaline phosphatase and BM purple

alkaline phosphatase substrate precipitating solution (Merck Roche) were used for staining. All samples were post-fixed with 4% PFA. Imaging of whole-mount samples was performed using a Zeiss AxioZoom with an Apotome module macroscope and sections were imaged using a Zeiss Axio Imager 2.

Ddi2 expression analysis in mouse embryos using qRT-PCR

RNA was isolated from frozen RNA later soaked tissue from the embryo from either *C57BL/6NCrl* or *Ddi2*^{ex6} strains using RNeasy plus Micro and Mini Kits (QIAGEN). Samples with RIN values above 7 in the Bioanalyzer RNA 6000 Nano assay (Agilent) were used for the synthesis of complementary DNA and RT controls using a reverse transcription TATAA GrandScript cDNA Synthesis Kit (TATAA Biocenter). qRT-PCR was performed using a LightCycler 480 (Roche) and TATAA SYBR GrandMaster Mix (TATAA Biocenter) by the Gene Core facility at the IBT CAS. Raw data were preprocessed using the GenEx program (MultiD Analyses AB). Primers are listed in Table S5.

Tissue lysis of Ddi2^{ex6} embryos for immunoblotting

Frozen embryos were homogenized in TSDG buffer (10 mM Tris/HCl pH 7.5, 25 mM KCl, 10 mM NaCl, 1 mM MgCl2, 0.1 mM EDTA, 0.5 mM DTT, 0.2 mM ATP, and 10% (v/v) glycerol) for 30 s at a frequency of 15 s^{-1} using a TissueLyser II (QIAGEN). As the tissue homogenates were to be used for both native and SDS PAGE, 3/5 of the sample was transferred to a new micro test tube and different inhibitors (10 mM NEM, 10 mM NaF, 1 mM Na_3VO_4, 2 mM $Na_4P_2O_7$, 10 μM MG132, and 1× cOmplete Mini protease inhibitor cocktail (EDTA free, Merck Roche) were added. Both homogenates were then lysed by four freezing and thawing cycles in liquid nitrogen. Lysates were centrifuged at 17,000 × g for 15 min at 4°C. The pellets were stored at −80°C until further analysis. Protein concentrations were determined using the Bradford reagent (0.01% (w/v) Coomassie brilliant blue G250, 4.8% (v/v) ethanol, and 8.5% phosphoric acid).

For detection of ubiquitinated proteins and transcription factors in the insoluble fraction, pellets of tissue lysate were resuspended in PBS with 5000 U/mL of *S. marcescens* endonuclease (Protean). After incubating for 10 min at room temperature while shaking, samples were denatured by adding SDS-PAGE sample buffer (final concentration: 62.5 mM Tris-HCl pH 6.8, 2% (w/v) SDS, 10% (v/v) glycerol, 1% β-mercaptoethanol, and 0.01% (w/v) bromophenol blue). The amount of lysis buffer added was calculated using the measured embryo weight, and 33 μL of buffer was added per 15 mg of embryo.

Experimental procedures with human cell lines

Cell extract preparation

For the preparation of whole cell extracts for immunoblotting, EAhy926 cells were grown in 35 mm or 60 mm dishes to 80−90% confluency, rinsed with ice-cold PBS, and lysed on the plate in RIPA lysis buffer (150 mM NaCl, 50 mM Tris-HCL (pH 8), 5 mM Na-EDTA (pH 8), 0.5% (v/v) NP-40, 0.5% (v/v) Triton X-100, 0.5% sodium dodecyl sulfate, 1 mM Na_3VO_4, 10 mM NaF, 2 mM $Na_4P_2O_7$, 10 μM MG132, 10 mM NEM and 1× cOmplete Mini protease inhibitor cocktail (EDTA free, Merck Roche)) for 5 min on ice. The cells were then scraped off the plate, lysates were collected in micro test tubes and kept on ice for 15 min followed by freezing at −80°C. Debris was removed by 15 min of centrifugation at 17,000 × g and 4°C.

For the preparation of cell extracts for native gel analysis, EAhy926 cells were grown in 35 mm dishes to 80−90% confluency. Cell pellets were lysed in TSDG buffer (10 mM Tris/HCl pH 7.5, 25 mM KCl, 10 mM NaCl, 1 mM MgCl2, 0.1 mM EDTA, 0.5 mM DTT, 0.2 mM ATP, and 10% (v/v) glycerol) by four freezing and thawing cycles in liquid nitrogen. Lysates were centrifuged at 17,000 × g for 15 min at 4°C and the supernatant was used for further analysis.

For the preparation of cell extracts for mass spectrometry, EAhy926 cells were grown in 60 mm dishes to 80−90% confluency. Cell pellets were lysed in RIPA lysis buffer (150 mM NaCl, 50 mM Tris-HCL (pH 8), 5 mM Na-EDTA (pH 8), 0.5% (v/v) NP-40, 0.5% (v/v) Triton X-100, 0.1% sodium dodecyl sulfate, 0.5% (v/v) sodium deoxycholate, 1 mM Na_3VO_4, 10 mM NaF, 2 mM $Na_4P_2O_7$, 10 μM MG132, 10 mM NEM and 1× cOmplete Mini protease inhibitor cocktail (EDTA free, Merck Roche)) by four freezing and thawing cycles (at −80°C). Lysates were centrifuged at 17,000 × g for 15 min at 4°C and the supernatant was used for further analysis.

Protein concentrations were determined using the Bradford reagent (0.01% (w/v) Coomassie brilliant blue G250, 4.8% (v/v) ethanol, and 8.5% phosphoric acid).

Cellular fractionation

EAhy926 cells were grown in 100 mm dishes to 80−90% confluency. All centrifugation steps were carried out at 4°C. Cell pellets were resuspended in 200 μL buffer A (20 mM Tris-HCL (pH 7.5), 10 mM KCl, 1.5 mM $MgCl_2$, 10% glycerol, 1 mM Na_3VO_4, 10 mM NaF, 10 μM MG132 and 1× cOmplete Mini protease inhibitor cocktail (EDTA free, Merck Roche)) and incubated on ice for 15 min before addition of 5 μL of NP-40 (12.5%). Samples were gently mixed immediately and incubated on ice for 5 min. After 10 min of centrifugation at 2,000 × g the supernatant was transferred to a new micro test tube and centrifuged again at 13,000 × g for 10 min. The cleared supernatant (non-nuclear fraction) was transferred to a new micro test tube. The pellet from the first centrifugation step was washed three times with 200 μL buffer A and centrifuged each time at 6,000 × g for 10 min. It was then resuspended in 50 μL buffer C (20 mM Tris-HCL (pH 7.5), 420 mM NaCl, 1.5 mM $MgCl_2$, 0.2 mM EDTA, 10% glycerol, 1 mM Na_3VO_4, 10 mM NaF, 10 μM MG132, and 1× protease inhibitor cocktail) and incubated on ice for 1 h, during which time the suspension was mixed every 10 min for 15 s. After 10 min of centrifugation at 13,000 × g the supernatant (nuclear fraction) was transferred to a new micro test tube. The insoluble pellet was mixed with 25 μL buffer E (20 mM Tris-HCL (pH 7.5), 150 mM NaCl, 1.5 mM $MgCl_2$,

5 mM CaCl2, 10% glycerol, 1 mM Na3VO4, 10 mM NaF, 10 μM MG132, and 1× protease inhibitor cocktail) and 1 μL Benzonase nuclease (250 U/μL, Sigma-Aldrich) and incubated on ice for 40 min, during which time the suspension was mixed every 10 min 25 μL buffer E/1 (buffer E + 2% SDS) was then added. The suspension was incubated at room temperature for 5 min and centrifuged at 13,000 × g for 10 min. The supernatant (chromatin-associated fraction) was transferred to a new micro test tube.

Protein concentrations were determined using the Bradford reagent (0.01% (w/v) Coomassie brilliant blue G250, 4.8% (v/v) ethanol, and 8.5% phosphoric acid). 30 μg total protein of each fraction was used for immunoblot analysis.

qRT-PCR of human cell cultures

To isolate RNA, EAhy926 cells were grown in 35 mm dishes to 80–90% confluency, rinsed with ice-cold PBS, and lysed on the dish in peqGOLD TriFastTM reagent (VWR Peqlab) for 5 min at room temperature. Lysates were transferred to micro test tubes and, if necessary, stored at −80°C before isolation of RNA according to the manufacturer's protocol. Complementary DNA was synthesized using 1.5 μg of RNA with random Oligo-dT-Primers (Promega) and M-MLV Reverse Transcriptase (Promega) according to the manufacturer's instructions. Real-time PCR was performed using Premix Ex Taq probe (Takara) and TaqMan assays (Applied Biosystems) with a CFX96TM Real-Time System (Bio-Rad).

Recombinant expression of mouse DDI2 proteins in human cell lines

Plasmids pTreTight (7.5 μg of plasmid DNA) were transfected into HEK293-TetOff-A2 cells at confluence of approx. 70% with opti-MEM medium (Thermo Fisher Scientific) and 10% (v/v) polyethylenimine (Sigma-Aldrich) and harvested 4, 8, 16, 24, 32, 40 and 48 h after transfection. Each treatment and time point were performed in triplicate.

Transfection with plasmid DNA

EAhy926 *DDI2* KO cells were grown in 35 mm dishes to 70% confluency and transfected with 50 ng of plasmid DNA and 950 ng of control plasmid (1 μg DNA in total) or control plasmid alone using jetPRIME (Polyplus) according to the manufacturer's protocol. 21 h after transfection, cells were treated with 500 nM BTZ for 3 h. Control plasmid pcDNA3.1 was purchased from Invitrogen. DDI2-V5-His (wild type) was previously cloned in the laboratory of Dr. Elke Krüger. Inactive mutant constructs DDI2 D252A[20] and DDI2 D252N (generated by site-directed mutagenesis in the laboratory of Dr. Grantz Saskova) were cloned into a pcDNA3.1/V5-His-TOPO vector backbone.

Protein analysis

Immunoblot analysis

For immunoblot analysis, 20–40 μg of embryo tissue lysates with inhibitors, 2–10 μL of insoluble pellet lysate or 10–40 μg of cell extracts were used for sodium dodecyl sulfate polyacrylamide gel electrophoresis (SDS PAGE). To analyze polyubiquitinated proteins, samples were separated on 4–14% Tris-Glycine gradient gels, whereas 10% or 12% Tris-Glycine gels were used for all other experiments. Proteins were transferred onto PVDF membranes (Merck Millipore) by wet electroblotting for 1 h at 100 V using the Mini-PROTEAN Tetra system (Bio-Rad). Equal protein loading was assessed by Amido Black staining (0.02% (m/v) Amido Black 10B, 9% (v/v) methanol, and 2% (v/v) acetic acid). Membranes were blocked with 1× ROTI Block (Carl Roth) and incubated overnight with the appropriate primary antibody. Excess antibody was removed by 3 × 5 min washing with 1× TBS-T (0.1% Tween 20). Membranes were then incubated for 30 min with a horseradish peroxidase-linked secondary antibody (anti-rabbit or anti-mouse IgG, Cell Signaling). The Clarity Western ECL Substrate (Bio-Rad) was used for chemiluminescent detection and membranes were visualized using Fusion FX (Vilber Lourmat) or RP NEW/UV film (CEA). If reprobing with another primary antibody was necessary, membranes were stripped using Restore Western Blot Stripping Buffer (Thermo Fisher Scientific) before blocking.

HEK293offA2 cells transfected with pTreTight plasmids were lysed in SDS sample buffer without dye (60 mM Tris pH 6.8, 60 nM SDS, and 0.3 mM β-mercaptoethanol) with cOmplete Mini, EDTA-free Protease Inhibitor Cocktail (Merck Roche) and 1 μL of (15× diluted) Benzonase (Novagen, Merck Millipore) by sonication on ice. Proteins were separated by SDS-PAGE electrophoresis and transferred to nitrocellulose membranes (Bio-Rad) using a wet transfer apparatus (Bio-Rad). Immunoblot analysis of protein expression was performed using protein-specific primary antibodies (anti-DDI2 (Bethyl) and anti-β-actin (Sigma Aldrich)) and fluorescent secondary antibodies using an Odyssey CLx Infrared Imaging System (LI-COR Biosciences).

Native gel analysis

Fresh embryo lysates without inhibitors or fresh native cell extracts were used for native PAGE analysis. Equal amounts of protein (15–20 μg) were mixed with 5× native PAGE sample buffer (final concentration: 50 mM Bis-Tris/HCl pH 6.8, 10% (v/v) glycerol, 50 mM NaCl, and 0.01% (w/v) bromophenol blue). Samples were loaded on 3–12% non-denaturing Bis-Tris gels (Invitrogen) and subjected to electrophoresis for 20 h at 45 V (4°C) using the Hoefer miniVE system (SE300-10A-1.0, Hoefer Pharmacia Biotech). The chymotrypsin-like activity of the proteasome was detected by incubating the gel in overlay buffer (20 mM Tris, 5 mM $MgCl_2$) containing 100 μM Suc-LLVY-AMC (Bachem) for 30 min at 37°C. Gels were analyzed using the Fusion FX (Vilber Lourmat) with an F-535 Y2 emission filter (530–550 nm). Proteasome complexes were subsequently blotted for 1 h at 200 V on ice onto PVDF membranes (Merck Millipore) and further handled as described above.

Mass spectrometry

Lysates of EAHy926 parental and DDI2 KO cells were processed following an adapted SP3 protocol (single pot solid-phase enhanced sample preparation) using hydrophobic and hydrophilic Sera-Mag SpeedBead magnetic particles (Cytiva).[114] Briefly, for each protein sample, 4 μg of protein were diluted with 20 mM Tris in a 1:2 ratio. Lysate reduction with 25 mM DTT at 37°C for 30 min was followed by alkylation with 100 mM iodoacetamide for 15 min in the dark, which was then quenched by addition of 25 mM DTT resulting in total sample volume 22 μL at this stage.

Samples were then mixed with the bead mixture in a 2:1 ratio. The suspension was diluted in 100% acetonitrile to a final concentration of 70% (v/v), mixed and incubated at 1.400 rpm and RT for 18 min. After 2 min incubation on the DynaMag-2 magnet (Thermo Fisher) the supernatant was discarded. Small molecule contaminants were removed by washing the beads twice with 180 μL 70% (v/v) ethanol and twice with 180 μL 100% acetonitrile. Beads were dried for 5 min and resuspended in 20 mM ammonium bicarbonate buffer. Protein digestion was performed with 160 ng trypsin (Promega; enzyme to protein ratio 1:25) at 37°C, overnight. Reaction was stopped and peptides precipitated on the beads by addition of 100% acetonitrile to a final concentration of 95% (v/v). After collection of the beads at the magnet, supernatant was discarded, beads were washed twice with 180 μL 100% acetonitrile and dried for 5 min. Peptide elution was achieved by resuspending beads in 10 μL of 2% (v/v) DMSO and incubation in an ultrasonic bath for 3 min. Beads were separated using the DynaMag-2 magnet (2 min). The supernatant (peptide solution) was transferred to a new microtube, and remaining beads were removed by a second application of the magnet. The final peptide solution was transferred to a vial with micro-insert and diluted with 10 μL 2× MS-buffer (4% acetonitrile, 0.2% acetic acid. Samples were stored at −80°C until measurement.

The acquisition of mass spectrometric data for relative quantitation was performed in data dependent mode using a QExactive HF Hybrid Quadrupole-Orbitrap mass spectrometer (Thermo Electron) coupled to a nano-LC system and controlled by Xcalibur software (Thermo Electron). Peptide pre-fractionation was carried out on a reverse phase column (Acclaim PepMap100, 75 μm inner diameter, 3 μm C18 particles, Thermo Scientific) using a 120 min-linear gradient from 5% to 25% acetonitrile in 0.1% acetic acid. Briefly, the data were acquired in the *m/z* range from 333 to 1650 *m/z*, the resolution for MS was 60,000 and for MS/MS 15,000. The AGC target was 3×10^6 for MS and 1×10^5 for MS/MS. Fragment spectra per cycle were acquired for the fifteen precursors with highest intensities in the MS scan. Precursors once selected were excluded from fragmentation for 30 s. For further details to the instrumental setup and the parameters for LC-MS/MS analysis, see Table S6.

For peptide and protein identification, raw spectra were searched against an Uniprot/SwissProt database (v. 2020_09) for human sequences within the Proteome Discoverer 2.4 software. Following conditions were applied: precursor mass tolerance: 10 ppm, fragment mass tolerance: 0.02 Da; two missed cleavage sites for trypsin as a proteolytic enzyme, static carbamidomethylation at cysteine, and variable modifications such as methionine oxidation, phosphorylation at serine or tyrosine, and acetylation of lysin. Acetylation, methionine-loss or a combination thereof were permitted as additional dynamic modification on protein N-termini. A peptide as well as protein FDR of 0.01 was used. Proteins were only considered identified, if two or more unique+razor peptides were found per protein.

QUANTIFICATION AND STATISTICAL ANALYSIS

Data were analyzed for quantification, statistic using ImageJ, GraphPad Prism 10 and the program R (version 3.6.2; 2019-12-12). Graphs were prepared using GraphPad Prism 10 or R, version 3.6.2 (2019-12-12). Statistical significance was marked with asterisks: * for a *p* value $\leq$0.05, ** for a *p* value $\leq$0,01, *** for a *p* value $\leq$0.001, **** for a *p* value $\leq$0,0001.

Expression of *Ddi2* in *C57BL/6NCrl* embryos was computed relative to expression of the *H2afz* housekeeping gene. In the qRT-PCR screen of 33 genes in *Ddi2*^{ex6} strain embryos, relative expression of genes was computed using normalization to *Tbp* and *H2afz* housekeeping genes with separately applied ANOVA statistical analysis (*p* value $\leq$0.05) and a linear mixed-effects model (LMM). Outliers were determined according to Grubbs's test. Bonferroni correction was applied to evaluate significance in both statistical approaches.

In the qRT-PCR screen of gene expression in EAhy926 cells, expression was calculated relative to expression of *RPLP0*. The Grubbs's outlier test was applied. Further statistical details about used, Mann-Whitney-test, unpaired t-test or two-way ANOVA can be found in the figure legends for individual experiments. At least a *p* value $\leq$0.05 was used. For details to native page analysis see Table S7.

Comparative quantitative protein analysis applied to mass spectrometry data were based on three biological replicates and performed in Proteome Discoverer 2.4 software (Thermo Fisher Scientific). *p* value was calculated by running the Tukey honestly significant difference test (post hoc) after application of variance test (ANOVA) for all conditions. Filter criteria for proteins with statistically significant difference in abundance were alteration by a factor of |1.5| and abundance ratio *p* value $\leq$0.05 or present in all replicates at one condition but not in the other (ON/OFF). These proteins were subjected to subsequent pathway analysis (Reactome v79).[115–117]